FISEVIER

Contents lists available at ScienceDirect

Journal of Computational Physics

www.elsevier.com/locate/jcp



A high order semi-implicit IMEX WENO scheme for the all-Mach isentropic Euler system



Sebastiano Boscarino a,*,1, Jing-Mei Qiu b,2, Giovanni Russo a, Tao Xiong c,3

- ^a Department of Mathematics and Computer Science, University of Catania, Catania, 95125, Italy
- ^b Department of Mathematical Sciences, University of Delaware, Newark, DE, 19716, USA
- ^c School of Mathematical Sciences, Fujian Provincial Key Laboratory of Mathematical Modeling and High-Performance Scientific Computing, Xiamen University, Xiamen, Fujian, 361005, PR China

ARTICLE INFO

Article history: Received 23 January 2019 Received in revised form 20 March 2019 Accepted 26 April 2019 Available online 6 May 2019

Keywords: Asymptotic preserving Semi-implicit IMEX WENO reconstruction Low-Mach Incompressible solver

ABSTRACT

In this paper, new high order schemes are constructed and analyzed, for the numerical solution of Euler equations of isentropic gas dynamics. Material waves are treated explicitly, while acoustic waves are treated implicitly, thus avoiding severe CFL restrictions for low Mach flows. High order accuracy in space is obtained by finite difference WENO schemes; while high order in time is obtained by IMEX methods with semi-implicit linearization treatment. The schemes are proven to be asymptotic preserving and asymptotic accurate as the Mach number vanishes. Several tests in one and two space dimensions illustrate the effectiveness of the proposed schemes.

© 2019 Elsevier Inc. All rights reserved.

1. Introduction

Development of numerical solvers for hyperbolic conservation laws has been an active field in the last few decades. Effective schemes, in capturing shocks and the entropy solution of a hyperbolic system, nowadays become a classic topic in the area of computational fluid dynamics [31,38,22,36,14]. Because of the hyperbolic nature, all such systems develop waves that propagate at finite speeds. In order to accurately compute all the waves in a hyperbolic system, one has to resolve all the space and time scales that characterize it. Most schemes devoted to such systems are obtained by explicit time discretization, and the time step has to satisfy a stability restriction, known as the CFL condition, which states that the time step should be limited by the size of the spatial mesh divided by the fastest wave speed (times a constant of order 1). Usually such a restriction is not a problem when the system is not stiff.

^{*} Corresponding author.

E-mail addresses: boscarino@dmi.unict.it (S. Boscarino), jingqiu@udel.edu (J.-M. Qiu), russo@dmi.unict.it (G. Russo), txiong@xmu.edu.cn (T. Xiong).

¹ S. Boscarino and G. Russo are members of the INdAM Research group GNCS. They have been partially supported by ITN-ETN Horizon 2020 Project ModCompShock (Modeling and Computation on Shocks and Interfaces) Project Reference 642768, by the Department of Mathematics and Computer Science, University of Catania Piano triennale della Ricerca 2016–2018, and by INdAM-GNCS 2018 project Numerical methods for multi-scale control problems and applications (n. prot. U-UFMBAZ-2018-000092 05-02-2018).

² Research is partially supported by NSF grant NSF-DMS-1522777 and 1818924, Air Force Office of Scientific Computing FA9550-18-1-0257.

³ Research is partially supported by NSFC grant 11601455, NSAF grant U1630247, NSF grant of Fujian Province No. 2016J05022 and the Fundamental Research Funds for the Central Universities No. 20720160009.

There are, however, cases when the system becomes stiff. As a prototype model, we consider the classical isentropic Euler equations of compressible gas dynamics. The system becomes stiff, when the Mach number becomes small: classical CFL condition on the time step determined by the acoustic waves deeply hinders the efficiency of numerical methods. On the other hand, one may be mainly interested in accurately capturing the motion of the fluid, without fully resolving acoustic waves. In such a case, one has to resort to implicit strategies for time discretization to avoid the acoustic CFL restriction. Naive implementation of implicit schemes for the solution of the Euler equations presents two kinds of problems. First, classical upwind discretization (say Godunov methods based on exact or approximate Riemann solvers) are highly nonlinear and very difficult to solve implicitly. Second, standard upwind schemes with numerical viscosities, which are inversely proportional to the Mach number, introduce excessive numerical dissipations on the slow wave, resulting in loss of accuracy [20]. Moreover, in the zero Mach number limit, the fluid model becomes an incompressible one with the divergence-free constraint on the velocity field. It is important that the numerical discretization follows such a constraint, as in well-developed incompressible fluid solvers [15,23,24].

Thus, there has been a great interest in developing numerical schemes that are efficient and effective for both the low Mach incompressible regime and for the compressible regime. For example, investigation of the effect on fully implicit schemes (and preconditioning techniques adopted to cure the large numerical diffusion) are discussed in [40] and in [32], both inspired by an early work of Turkel [39]. One of the first works, in which semi-implicit calculation of the pressure is incorporated in a compressible flow, is given by Casulli and Greenspan [12], in which the authors use an upwind discretization on the material flow, and an implicit equation for the pressure, which is solved by a SOR-type method. Several authors have subsequently worked on the development of semi-implicit methods [29,33] base on low-Mach asymptotic [28]; such schemes are specifically designed to deal with low Mach regimes. However, when the Mach number is not small, then shock discontinuities may form. In these cases, it is necessary to resort to conservative schemes (see for example [25] and [19] for isentropic Euler and Navier-Stokes equations, or [16] for full Euler and Navier-Stokes case). Most shock capturing all Mach-number schemes, presented in the literature, are based on the finite volume method and are usually restricted to second order accuracy in space and time, for example [21,11], with an exception represented by the paper [37]. In [37], the authors adopt a space-time discontinuous Galerkin method for all Mach-number flow, which involves staggered meshes and Picard iterations for solving large nonlinear systems.

The aim of the present paper is to propose a new simple framework to design a conservative high order finite difference scheme for the compressible isentropic Euler equations with Mach number ranging from zero to order one. Such new framework does not involve splitting parameter as in [25,19], yet the asymptotic consistency and high order accuracy can be proved in the zero Mach number limit for the incompressible Euler equations. The method is based on a conservative finite-difference formulation on a single mesh. Convective terms are treated explicitly by a suitable local Lax-Friedrich flux, while acoustic terms are treated implicitly with zero numerical diffusion, thus achieving at the same time good accuracy and low numerical diffusion. The first order version of our scheme is consistent with the one proposed recently in [21]; here in this paper, we generalize the scheme in the finite difference framework to high order accuracy in space by using the finite difference weighted essentially non-oscillatory (WENO) techniques, and in time with high order semi-implicit linearization strategy.

The plan of the paper is the following. After the introductory section, we recall the isentropic Euler equations, and how they relax to the incompressible Euler equations as the Mach number vanishes. Section 3 is devoted to the presentation and analysis of the schemes: the basic first order accurate scheme in time is introduced, and an accurate linear stability analysis is performed. Later we illustrate how to extend the scheme to higher order both in time and space. Section 4 concerns with the analysis of the AP property of the scheme. The next section presents several numerical tests in one and two space dimensions. In the last section we draw conclusions and mention some work in progress. In the Appendix, we present the AP property of the semi-implicit linearized scheme, as well as the IMEX Butcher tableaux adopted in simulations presented in this paper.

2. The isentropic Euler system for all-Mach number

We consider the isentropic Euler equations

$$\rho_t + \nabla \cdot \mathbf{q} = 0, \tag{2.1a}$$

$$\rho_t + \nabla \cdot \mathbf{q} = 0, \tag{2.1a}$$

$$\mathbf{q}_t + \nabla \cdot \left(\frac{\mathbf{q} \otimes \mathbf{q}}{\rho}\right) + \nabla p(\rho) = 0, \tag{2.1b}$$

where $x \in \Omega \subset \mathbb{R}^d$, $t \ge 0$, ρ is the density of the fluid, \mathbf{u} is the velocity of the fluid, p is the pressure and $\mathbf{q} = \rho \mathbf{u}$ is the momentum. Here we consider a polytropic gas, for which the equation of state takes the form: $p(\rho) = C\rho^{\gamma}$ where C(s)depends on the entropy (which is assumed to be constant) and $\gamma = C_p/C_v$ is the polytropic constant.

In order to describe the low Mach number limit, we rescale the equations considering the following reference quantities: ρ_0 , u_0 , p_0 , x_0 , t_0 , with $u_0 = x_0/t_0$ where the dimensionless variables are then given by:

$$\hat{x} = x/x_0$$
, $\hat{t} = t/t_0$, $\hat{\rho} = \rho/\rho_0$, and $\hat{u} = u/u_0$.

Inserting these expressions into the equations (2.1) (and omitting the hat) one obtains the rescaled (non-dimensionalised) isentropic Euler equations:

$$\rho_t + \nabla \cdot \mathbf{q} = 0, \tag{2.2a}$$

$$\mathbf{q}_t + \nabla \cdot \left(\frac{\mathbf{q} \otimes \mathbf{q}}{\rho}\right) + \frac{1}{\varepsilon^2} \nabla p(\rho) = 0, \tag{2.2b}$$

where $\varepsilon = u_0 \sqrt{\rho_0/p_0}$ is proportional to the Mach number. System (2.2) is *hyperbolic* and the eigenvalues in direction ${\bf n}$ are: $\lambda_1 = {\bf u} \cdot {\bf n} - c/\varepsilon$, $\lambda_2 = {\bf u} \cdot {\bf n} + c/\varepsilon$ with $c = \sqrt{\gamma p/\rho}$ being the sound speed. Throughout the paper, we denote by *acoustic* waves that perturbations traveling with the speed of sound c, and *material waves* the perturbations carried by the fluid, thus moving at speed ${\bf u}$. For boundary conditions, we assume ${\bf u} \cdot {\bf n} = 0$ on $\partial \Omega$, or assume Ω is \mathbb{T}^d , i.e. periodic boundary conditions.

Now we recall the classical formal derivation of the incompressible Euler equations from the isentropic compressible Euler system (2.2) [28]. To determine the asymptotic behavior as $\varepsilon \to 0$, we consider an asymptotic expansion *ansatz* for the following variables:

$$\rho(x,t) = \rho_0(x,t) + \varepsilon^2 \rho_2(x,t) + \cdots,$$

$$p(x,t) = p_0(x,t) + \varepsilon^2 p_2(x,t) + \cdots,$$

$$\mathbf{u}(x,t) = \mathbf{u}_0(x,t) + \varepsilon^2 \mathbf{u}_2(x,t) + \cdots,$$
(2.3)

Inserting (2.3) into (2.2), to $\mathcal{O}(\varepsilon^{-2})$, one gets, in the momentum conservation equation (2.2):

$$\nabla p_0 = 0$$
.

Therefore, $p_0(x,t) = p_0(t)$, and by $p = p(\rho)$, we have $\rho_0 = \rho_0(t)$, i.e. to lower order in ε , density and pressure are constants in space. Next, by taking the $\mathcal{O}(1)$ terms, we have

$$\partial_t \rho_0 + \nabla \cdot (\rho_0 \mathbf{u}_0) = 0$$
 (2.4a)

$$\partial_t(\rho_0 \mathbf{u}_0) + \nabla \cdot (\rho_0 \mathbf{u}_0 \otimes \mathbf{u}_0) + \nabla p_2 = 0, \tag{2.4b}$$

where p_2 as appearing in (2.3) is the hydrostatic pressure. Now, the incompressibility is forced by using the boundary conditions to solve system (2.2) on the domain Ω with $\mathbf{u} \cdot \mathbf{n} = 0$ on $\partial \Omega$ or periodic boundary conditions. Because $\rho_0 = \rho_0(t)$ for (2.4) one has:

$$\nabla \cdot \mathbf{u}_0 = -\frac{1}{\rho_0} \frac{d\rho_0}{dt}.$$

Integrating on Ω one has:

$$-|\Omega| \frac{1}{\rho_0} \frac{d\rho_0}{dt} = \int\limits_{\Omega} \nabla \cdot \mathbf{u}_0 d\Omega = \int\limits_{\partial\Omega} \mathbf{u}_0 \cdot \mathbf{n} ds = 0, \tag{2.5}$$

due to the boundary conditions. Therefore ρ_0 remains constant in space and in time, so that $\nabla \cdot \mathbf{u}_0 = 0$, and (2.4b) becomes

$$\partial_t \mathbf{u}_0 + \nabla \cdot (\mathbf{u}_0 \otimes \mathbf{u}_0) + \nabla p_2 = 0, \tag{2.6}$$

where p_2 plays the role of Lagrangian multiplier in enforcing the divergence-free condition of the velocity field. To see this, taking the divergence of the equation (2.6) and using the incompressibility, one obtains

$$-\Delta p_2 = \nabla^2 : (\rho_0 \mathbf{u}_0 \otimes \mathbf{u}_0), \tag{2.7}$$

where ∇^2 and : are respectively the tensor of second order derivatives and the contracted product of two tensors.

As observed in [28], we assume that the initial condition for the problem is *well-prepared* which means that the initial condition for (2.3) is compatible with the equations at various orders of ε . In our case, well-prepared initial conditions are obtained by imposing

$$\rho(x,0) = \rho_0 + \varepsilon^2 \rho_2(x),$$

$$\mathbf{u}(x,0) = \mathbf{u}_0(x) + \mathcal{O}(\varepsilon),$$
(2.8)

with ρ_0 constant and $\nabla \cdot \mathbf{u}_0 = 0$. Then, compatibility with the equations at order zero in ε is given by:

$$\rho(x,0) = Const,$$

$$\nabla \cdot \mathbf{u}_0 = 0,$$

$$\partial_t \mathbf{u}_0 + (\mathbf{u}_0 \cdot \nabla)\mathbf{u}_0 + \frac{\nabla p_2}{\rho_0} = 0.$$
(2.9)

Well-prepared initial conditions are clearly explained in [8] or in the classical book by Hairer and Wanner ([26], Chap. VI). Note that well-prepared initial conditions are required if we want that the solution to the ε -dependent problem smoothly converges to the solution of the limit incompressible problem. For an arbitrary initial condition, an initial layer will appear, which require a numerical resolution at the ε -scale.

Finally, from a numerical point of view, when the Mach number is very small, standard explicit shock-capturing methods require a CFL time restriction dictated by the sound speed c/ε to integrate the system. This leads to the stiffness in time, ([25], [19], [16], where the time discretization is constrained by a stability condition given by

$$\Delta t < \Delta x / \lambda_{\text{max}} \approx \mathcal{O}(\varepsilon \Delta x),$$
 (2.10)

since $\lambda_{\max} = \max_{\Omega} (|\mathbf{u}| + c/\varepsilon)$.

This restriction results in an increasingly large computational time for small ε . The second drawback is due to the excessive numerical viscosity of standard upwind schemes, that scales as ε^{-1} , leading to highly inaccurate solutions. Thus, it is crucial to design schemes with asymptotic stability and consistency in the incompressible limit, i.e. the *asymptotic preserving* (AP) property.

3. Numerical schemes

We aim to construct and analyze a new class of high order finite difference schemes with the AP property for unsteady compressible flows when the Mach number ε spans several orders of magnitude. The features of our scheme are the following: we design an implicit-explicit time discretization strategy, so that the scheme is stable with a time stepping constraint independent of the Mach number ε , the AP property is preserved in the zero Mach number limit and the scheme can be implemented in a semi-implicit manner [6,5,4,7] to enable effective and efficient numerical implementations; meanwhile we adopt high order WENO spatial discretization strategies, so that the scheme can successfully capture shocks in the compressible regime; our scheme can preserve the incompressible velocity field in the zero Mach number limit by involving an elliptic solver for the hydrostatic pressure. The organization of this section is the following: we will first present a first order discretization both in time and in space; and then discuss high order extensions afterwards.

3.1. Set up a first order scheme

We first propose an effective first order time discretization with proper implicit and explicit treatments, which is similar to that in the recent work [21].

$$\begin{cases}
\frac{\rho^{n+1} - \rho^n}{\Delta t} + \nabla \cdot \mathbf{q}^{n+1} = 0, \\
\frac{\mathbf{q}^{n+1} - \mathbf{q}^n}{\Delta t} + \nabla \cdot \left(\frac{\mathbf{q} \otimes \mathbf{q}}{\rho}\right)^n + \frac{1}{\varepsilon^2} \nabla p(\rho^{n+1}) = 0.
\end{cases}$$
(3.11)

Substituting \mathbf{q}^{n+1} in the first sub-equation of (3.11) by the expression from the second sub-equation, one gets

$$\begin{cases}
\frac{\rho^{n+1} - \rho^n}{\Delta t} + \nabla \cdot \mathbf{q}^n - \Delta t \nabla^2 : \left(\frac{\mathbf{q} \otimes \mathbf{q}}{\rho}\right)^n - \frac{\Delta t}{\varepsilon^2} \Delta p(\rho^{n+1}) = 0, \\
\frac{\mathbf{q}^{n+1} - \mathbf{q}^n}{\Delta t} + \nabla \cdot \left(\frac{\mathbf{q} \otimes \mathbf{q}}{\rho}\right)^n + \frac{1}{\varepsilon^2} \nabla p(\rho)^{n+1} = 0.
\end{cases}$$
(3.12)

Notice that although the pressure term appears to be the only stiff term in the isentropic Euler system, the implicit treatment on the advection term $\nabla \cdot \mathbf{q}^{n+1}$ in the first sub-equation of (3.11) is necessary to preserve the AP property. Indeed, an explicit treatment of $\nabla \cdot \mathbf{q}$ term in the first equation of (3.11) would make the whole method explicit, and prone to a severe ε -dependent stability restriction. We would also like to emphasize the following: although the two semi-discrete systems (3.11) and (3.12) appear to be mathematically equivalent, system (3.12) offers a simpler and more compact framework, when spatial discretizations are applied. In fact, it is crucial that we perform our spatial discretization based on the system (3.12), instead of (3.11), because in this way it is easier to obtain a compact and high order discretization of second order derivative.

The AP property for the time discretization (3.12) has been discussed in [21]. Pluggin formal expansions (2.3) into scheme (3.12) and collecting equal powers of ε , with proper boundary conditions, we have

$$\mathcal{O}(1/\varepsilon^2)$$
 terms: $\Delta p(\rho_0^{n+1}) = 0$, i.e. $p_0 \equiv const$, $\rho_0 \equiv const$, (3.13)

$$\mathcal{O}(1) \quad \text{terms}: \quad \begin{cases} \nabla \cdot \mathbf{q}_0^n - \Delta t \nabla^2 : \left(\frac{\mathbf{q}_0 \otimes \mathbf{q}_0}{\rho_0}\right)^n - \Delta t \Delta p_2^{n+1} = 0, \\ \frac{\mathbf{q}_0^{n+1} - \mathbf{q}_0^n}{\Delta t} + \nabla \cdot \left(\frac{\mathbf{q}_0 \otimes \mathbf{q}_0}{\rho_0}\right)^n + \nabla p_2^{n+1} = 0. \end{cases}$$

$$(3.14)$$

Eq. (3.14) can be derived by collecting equal powers of order one terms, and from the fact that p_0 and ρ_0 are constants from eq. (3.13). It can be seen that eq. (3.13) implies that the fluid density stays constant. Meanwhile, when one takes the divergence of the second sub-equation in system (3.14), it can be seen that \mathbf{q}_0^{n+1} is divergence free. In particular, the first sub-equation in (3.14) plays the role of divergence cleaning for the updated \mathbf{q}_0^{n+1} in the second sub-equation of (3.14). That is to say, in the zero Mach number limit, the fluid flow is incompressible with constant fluid density and divergence-free velocity field. In fact, eq. (3.14) provides a scheme to discretize the incompressible Euler system (2.4) with a divergence cleaning step, which shares similar spirits to the classical projection methods [13,2,27,18]. Also see [30] for a review and comparison for different approaches solving incompressible flows.

Remark 3.1. Our strategy of numerical discretizations is different from the traditional method-of-lines discretization. The method-of-line approach involves discretization in space first; and then solving the resolving time-dependent problem as an ODE system; while here for all-Mach problem (similarly for many other temporal multi-scale problems) we do the opposite. Specifically, we first perform time discretization to ensure AP property, after which we propose to apply proper spatial discretizations.

Next we describe a first order finite difference scheme to illustrate the basic principle in our spatial discretization. Notice that our numerical solutions for all primal variables are on collocated grid, which is different from the staggered mesh treatment adopted in [11], and from the zone-centered or face-centered variables used in [37].

1. Spatial discretization of convective terms $\nabla \cdot \mathbf{q}^n$ and $\nabla \cdot (\mathbf{q} \otimes \mathbf{q}/\rho)^n$ in eq. (3.12) can be treated by standard upwind strategy (e.g., by using a local Lax-Friedrichs flux). For example, $\nabla \cdot \mathbf{q}$ would be approximated by a flux-difference form,

$$D_{up} \cdot \mathbf{q} \doteq \frac{1}{\Delta x} (\hat{q}_{i+\frac{1}{2},j}^1 - \hat{q}_{i-\frac{1}{2},j}^1) + \frac{1}{\Delta y} (\hat{q}_{i,j+\frac{1}{2}}^2 - \hat{q}_{i,j-\frac{1}{2}}^2), \quad \mathbf{q} = (q^1, q^2)$$

with the flux functions

$$\hat{q}_{i+\frac{1}{2},j}^{1} = \frac{1}{2}(q_{i,j}^{1} + q_{i+1,j}^{1}) + \frac{\alpha_{1,i,j}}{2}(\rho_{i,j} - \rho_{i+1,j}), \quad \hat{q}_{i,j+\frac{1}{2}}^{2} = \frac{1}{2}(q_{i,j}^{2} + q_{i,j+1}^{2}) + \frac{\alpha_{2,i,j}}{2}(\rho_{i,j} - \rho_{i,j+1}),$$

where $\alpha_{1,i,j}$ and $\alpha_{2,i,j}$ are maximum flow speed in x- and y-directions respectively. Here D_{up} denotes an upwind discretization. The spatial discretization of $\nabla \cdot (\mathbf{q} \otimes \mathbf{q}/\rho)^n$ can be approximated in a similar manner by $D_{up} \cdot (\mathbf{q} \otimes \mathbf{q}/\rho)^n$, as in a standard finite difference solver for compressible flows. In particular, here we use a conservative finite difference formulation with a local Lax-Friedrich flux splitting [36].

2. Spatial discretization of second-derivative terms $\nabla^2: (\mathbf{q}\otimes\mathbf{q}/\rho)^n$ and $\Delta p(\rho^{n+1})$. These second-derivative terms could be discretized by a high order central difference approximation by $D_0^2: (\mathbf{q}\otimes\mathbf{q}/\rho)^n$ and $D_\Delta(p^{n+1})$ respectively. In particular, a second order discretization of $\nabla^2: (\mathbf{q}\otimes\mathbf{q}/\rho)$ by $D_0^2: (\mathbf{q}\otimes\mathbf{q}/\rho)$ is the following

$$D_{0}^{2}: \left(\frac{\mathbf{q} \otimes \mathbf{q}}{\rho}\right) \doteq D_{xx} \left(\frac{(q^{1})^{2}}{\rho}\right) + 2D_{xy} \left(\frac{q^{1}q^{2}}{\rho}\right) + D_{yy} \left(\frac{(q^{2})^{2}}{\rho}\right)$$

$$\doteq \frac{1}{\Delta x^{2}} \left(\left(\frac{(q^{1})^{2}}{\rho}\right)_{i+1,j} - 2\left(\frac{(q^{1})^{2}}{\rho}\right)_{i,j} + \left(\frac{(q^{1})^{2}}{\rho}\right)_{i-1,j}\right)$$

$$+ \frac{1}{2\Delta x\Delta y} \left(\left(\frac{q^{1}q^{2}}{\rho}\right)_{i+1,j+1} - \left(\frac{q^{1}q^{2}}{\rho}\right)_{i-1,j+1}\right)$$

$$- \left(\left(\frac{q^{1}q^{2}}{\rho}\right)_{i+1,j-1} - \left(\frac{q^{1}q^{2}}{\rho}\right)_{i-1,j-1}\right)\right)$$

$$+ \frac{1}{\Delta y^{2}} \left(\left(\frac{(q^{2})^{2}}{\rho}\right)_{i,j+1} - 2\left(\frac{(q^{2})^{2}}{\rho}\right)_{i,j} + \left(\frac{(q^{2})^{2}}{\rho}\right)_{i,j-1}\right),$$

a second order discretization of the Laplace operator Δp by $D_{\Delta}(p)$ is the following

$$\frac{p_{i+1,j}-2p_{i,j}+p_{i-1,j}}{\Delta x^2}+\frac{p_{i,j+1}-2p_{i,j}+p_{i,j-1}}{\Delta y^2}.$$

3. Spatial discretization of ∇p^{n+1} in the second sub-equation of (3.12). A central difference without numerical diffusion is proposed to approximate ∇p ,

$$D_0(p) \doteq \left(\frac{p_{i+1,j} - p_{i-1,j}}{2\Delta x}, \frac{p_{i,j+1} - p_{i,j-1}}{2\Delta y}\right)^T.$$

Notice that it is essential that *no* numerical diffusion will be introduced for this term. Otherwise, the numerical diffusion will scale as $\mathcal{O}(1/\epsilon^2)$, strongly polluting numerical solutions at small values of ϵ . Note that $D_0^2 \neq D_0 D_0$.

In summary, a first order fully discretized scheme for solving (3.12) is proposed as

$$\begin{cases}
\frac{\rho^{n+1} - \rho^n}{\Delta t} + D_{up} \cdot \mathbf{q}^n - \Delta t D_0^2 : \left(\frac{\mathbf{q} \otimes \mathbf{q}}{\rho}\right)^n - \frac{\Delta t}{\varepsilon^2} D_{\Delta}(p(\rho^{n+1})) = 0, \\
\frac{\mathbf{q}^{n+1} - \mathbf{q}^n}{\Delta t} + D_{up} \cdot \left(\frac{\mathbf{q} \otimes \mathbf{q}}{\rho}\right)^n + \frac{1}{\varepsilon^2} D_0(p(\rho)^{n+1}) = 0.
\end{cases}$$
(3.15)

To solve the system (3.15), we first solve ρ^{n+1} from equation (3.15) implicitly as *a nonlinear elliptic equation*; then we update the momentum from the second equation of (3.15) from an explicit calculation. A semi-implicit approach with linearization of the pressure term in the first sub-equation of the system (3.15) is possible as discussed later in Section 3.3.

3.2. Linearized stability analysis

In this section we present a stability analysis for the scheme (3.12) applied to the one dimensional linearized isentropic system. First of all we consider the system in 1D

$$\begin{cases} \rho_t + q_x = 0, \\ q_t + \left(\frac{q^2}{\rho} + \frac{1}{\varepsilon^2} p(\rho)\right)_x = 0, \end{cases}$$
(3.16)

denoting $q = \rho u$

So, we rewrite system (3.16) by linearizing it around the constant state $\rho_0 = 1$, $u_0 = 1$ and $p_0 = 1$. This leads to

$$\begin{cases} \rho_t + q_x = 0 \\ q_t + 2q_x + (\frac{1}{\varepsilon^2} - 1)\rho_x = 0. \end{cases}$$
 (3.17)

We assume that the domain is $[0, 2\pi]$ with periodic boundary conditions.

Applying time discretization (3.12) to (3.17), and discretizing space with local Lax-Friedrich flux we obtain:

$$\rho_{j}^{n+1} = \rho_{j}^{n} - \mu \left(\tilde{D}_{x}(q^{n}) - \frac{\alpha}{2} \tilde{D}_{xx}(\rho^{n}) \right)_{j} + \mu^{2} \tilde{D}_{xx}(2q^{n} - \rho^{n})_{j} + \frac{\mu^{2}}{\varepsilon^{2}} \tilde{D}_{xx}(\rho^{n+1})_{j}$$

$$q_{j}^{n+1} = q_{j}^{n} - \mu \left(\tilde{D}_{x}(2q^{n} - \rho^{n}) - \frac{\alpha}{2} \tilde{D}_{xx}(q^{n}) \right)_{j} - \frac{\mu}{\varepsilon^{2}} \tilde{D}_{x}(\rho^{n+1})_{j}$$
(3.18)

with $\mu = \Delta t/\Delta x$ and we made use of undivided difference operators

$$\tilde{D}_x h_j = \frac{h_{j+1} - h_{j-1}}{2}, \quad \tilde{D}_{xx} h_j = h_{j+1} - 2h_j + h_{j-1}.$$

We apply the Von Neumann analysis to access the stability property of the proposed first order scheme. We express every quantity $U_j^n = (\rho_j^n, q_j^n)$ by a Fourier series in space, where $i^2 = -1$, $U_j^n = \sum_{k \in \mathbb{Z}} \hat{U}_k^n \exp(ikj\Delta x)$. The evolution of each Fourier mode \hat{U}_k is obtained by observing that $\tilde{D}_x e^{ij\xi} = i\sin\xi e^{ij\xi}$, $\tilde{D}_{xx}e^{ij\xi} = 2(\cos\xi - 1)e^{ij\xi}$ with $\xi = k\Delta x$, with integer k. Then we get

$$A\hat{U}_k^{n+1} = B\hat{U}_k^n$$

with

$$A = \begin{pmatrix} 1 + \frac{\mu^2}{\varepsilon^2} 2(1 - \cos \xi) & 0 \\ \frac{\mu i \sin \xi}{\varepsilon^2} & 1 \end{pmatrix}$$

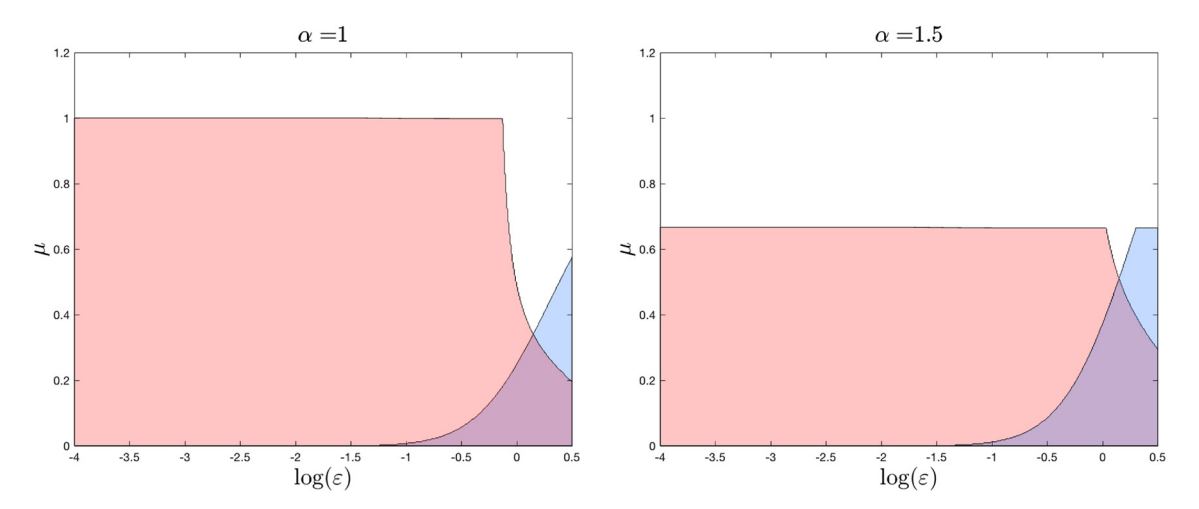


Fig. 3.1. Stability region in the $\varepsilon - \mu$ plane with $\alpha = 1$ (left panel) and $\alpha = 1.5$ (right panel). Red area represents the stability region for the proposed implicit-explicit approach, blue area for the fully explicit one. (For interpretation of the colors in the figure(s), the reader is referred to the web version of this article.)

and

$$B = \begin{pmatrix} 1 + \mu(\alpha - 2\mu)(\cos \xi - 1) & -i\mu\sin \xi + 4\mu^2(\cos \xi - 1) \\ \mu i\sin \xi & 1 - 2i\mu\sin \xi + \alpha\mu(\cos \xi - 1) \end{pmatrix}.$$

We compute the quantity

$$\mathcal{F}(\alpha, \mu, \varepsilon) := \max_{\xi \in [-\pi, \pi]} (\max(|\lambda_{+}(\xi)|, |\lambda_{-}(\xi)|)),$$

where $\lambda_{\pm}(\xi)$ denote the roots of the characteristic polynomial: $p(\lambda; \alpha, \mu, \varepsilon) = \det(\lambda A - B)$. For fixed values of α , we plot in Fig. 3.1 the stability region (red regions) in the $\varepsilon - \mu$ plane, in which

$$|\mathcal{F}(\alpha,\mu,\varepsilon)| < 1. \tag{3.19}$$

We consider two values of α : $\alpha=1$ (left panel) and $\alpha=1.5$ (right panel). In the same plots, the stability region of a fully explicit scheme is also plotted (blue regions) for comparison. It is observed that, the scheme is uniformly stable for small values of ε ; when the Mach number $\varepsilon \geq 1$, the explicit scheme has better stability property than the semi-implicit one that we proposed. Stability properties for the Euler system with $\varepsilon \geq 1$ are subject to further investigation.

3.3. High order extensions in temporal discretization

Next we present and describe two different approaches for solving (2.2), i.e., the nonlinearly implicit IMEX-RK methods (NI IMEX RK) and the semi-implicit IMEX-RK ones (SI-IMEX RK). The NI IMEX RK schemes are based on the classical IMEX-RK framework ([3,34,9]), while the SI IMEX RK schemes [6] come from a semi-implicit variant of the additive Runge-Kutta (ARK) approach [41]. Here we first discretize in time using IMEX methods, while keeping the spatial derivatives continuous with the understanding that proper high order discretization will be applied, as discussed in the following subsection 3.4. This is in contrast with the traditional method-of-lines approach which first discretize in space and then in time. Such strategy allows for a compact discretization of the second order derivative terms as in (3.12). In particular, on each IMEX-RK stage, as in the first order IMEX case, we plug the second sub-equation for $\bf q$ into the first sub-equation for ρ (as in eq. (3.11)) and obtain an equivalent system (as in (3.12)), which allows a compact discretization of second order derivatives terms in the system (3.12).

1. IMEX-RK formulation. An s-stage IMEX-RK scheme is represented by the double Butcher tableau:

$$\frac{\tilde{c} \mid \tilde{A}}{\mid \tilde{b}^T \mid} \frac{c \mid A}{\mid b^T \mid} \tag{3.20}$$

where \tilde{A} , $A \in \mathbb{R}^{s \times s}$, \tilde{c} , c, \tilde{b} , $b \in \mathbb{R}^{s}$. The coefficients \tilde{c} and c, are related to matrices \tilde{A} and A by the relations

$$\tilde{c} = \sum_{j=1}^{i-1} \tilde{a}_{ij}, \quad c = \sum_{j=1}^{i} a_{ij}.$$

Matrix $\tilde{A} = (\tilde{a}_{ij})$ is an *explicit* triangular matrix with zero elements on the main diagonal. For computational efficiency, we restrict our consideration to *diagonally implicit* matrices $A = (a_{ij})$ with $a_{ij} = 0$, for j > i. We rewrite the isentropic Euler system for $U = (\rho, \mathbf{q})$ in the following form

$$U_t = F(U) + G(U),$$
 (3.21)

where $F(U) = -\left(0, \nabla \cdot \left(\frac{\mathbf{q} \otimes \mathbf{q}}{\rho}\right)\right)^T$ is treated explicitly and $G(U) = -\left(\nabla \cdot \mathbf{q}, \frac{1}{\varepsilon^2} \nabla p(\rho)\right)^T$ is treated implicitly by an IMEX-RK scheme with coefficients specified in Butcher tableau (3.20). For example, applying the first order IMEX, see the tableau (B.1), gives a first order time discretization formulated in eq. (3.11). In general, applying a high order IMEX-RK scheme to (3.21) gives:

$$\mathbf{U}^{(i)} = \mathbf{U}^{n} + \Delta t \sum_{j=1}^{i-1} \tilde{a}_{ij} F(\mathbf{U}^{(j)}) + \Delta t \sum_{j=1}^{i-1} a_{ij} G(\mathbf{U}^{(j)}) + \Delta t a_{ii} G(\mathbf{U}^{(i)}),$$

$$\mathbf{U}^{n+1} = \mathbf{U}^{n} + \Delta t \sum_{i=1}^{s} \tilde{b}_{i} F(\mathbf{U}^{(i)}) + \Delta t \sum_{i=1}^{s} b_{i} G(\mathbf{U}^{(i)}).$$
(3.22)

Similar to the first order IMEX-RK case, we want to rewrite the system in the form of eq. (3.12) so that a compact discretization of second order derivative terms are possible. We can first update the stage values of ρ , then use it to update ${\bf q}$ in a stage-by-stage manner, provided that the implicit part is diagonally implicit. A nonlinear Newton's iteration can be used to solve the nonlinear system of ρ^{n+1} ; thus we call this method "nonlinearly implicit" (NI) IMEX-RK. In particular, to update the solutions from t^n to t^{n+1} by NI-IMEX RK, we use the following flow chart of the algorithm:

(a) Compute the stage values for $i = 1, \dots, s$

$$\rho^{(i)} = \rho^{n} - \Delta t \sum_{j=1}^{i-1} a_{ij} \nabla \cdot \mathbf{q}^{(j)} - \Delta t a_{ii} \nabla \cdot \mathbf{q}^{n}$$

$$+ a_{ii} \Delta t^{2} \left(\sum_{j=1}^{i-1} \tilde{a}_{ij} \nabla^{2} : \left(\frac{\mathbf{q} \otimes \mathbf{q}}{\rho} \right)^{(j)} + \sum_{j=1}^{i-1} a_{ij} \frac{1}{\varepsilon^{2}} \Delta p(\rho^{(j)}) \right)$$

$$+ \frac{1}{\varepsilon^{2}} \Delta t^{2} (a_{ii})^{2} \Delta p(\rho^{(i)}),$$

$$\mathbf{q}^{(i)} = \mathbf{q}^{n} - \Delta t \left(\sum_{k=1}^{i-1} \tilde{a}_{ij} \nabla \cdot \left(\frac{\mathbf{q} \otimes \mathbf{q}}{\rho} \right)^{(j)} + \sum_{k=1}^{i} a_{ij} \Delta p(\rho^{(j)}) \right);$$

$$(3.23)$$

(b) Update the solution by taking linear combination of right hand side functions at stage values:

$$\rho^{n+1} = \rho^n - \Delta t \sum_{i=1}^s b_i \nabla \cdot \mathbf{q}^{(i)},$$

$$\mathbf{q}^{n+1} = \mathbf{q}^n - \Delta t \left(\sum_{i=1}^s \tilde{b}_i \nabla \cdot \left(\frac{\mathbf{q} \otimes \mathbf{q}}{\rho} \right)^{(i)} + \sum_{i=1}^s b_i \nabla p(\rho^{(i)}) \right).$$
(3.24)

2. A semi-implicit linearized treatment. Direct application of IMEX-RK methods to (3.21) requires solving a nonlinear system due to the nonlinear relation between p and ρ ($p = \rho^{\gamma}$ for $\gamma \neq 1$). To avoid excessive computational effort in solving nonlinear systems, we propose to adopt the semi-implicit approach proposed in [6] that allows a linearization, while maintaining high order truncation error of the original IMEX-RK scheme. For example, a first order semi-implicit treatment reads

$$\frac{\rho^{n+1} - \rho^n}{\Delta t} + \nabla \cdot \mathbf{q}^n - \Delta t \nabla^2 : \left(\frac{\mathbf{q} \otimes \mathbf{q}}{\rho}\right)^n - \frac{\Delta t}{\varepsilon^2} \nabla \cdot \left(p'(\rho^n) \nabla \rho^{n+1}\right) = 0. \tag{3.25}$$

The procedure can be extended to high order using IMEX-RK schemes from the literature. A list of schemes adopted in the paper is summarized in the Appendix B.

Following [6], the idea is to write system (2.2) as an autonomous system

$$U' = \mathcal{H}(U, U)$$

where $\mathcal{H}: \mathbb{R}^m \times \mathbb{R}^m \to \mathbb{R}^m$ is a sufficiently regular mapping. We assume that an explicit treatment to the first argument of \mathcal{H} (using subscript "I"), and an implicit treatment to the second argument (using subscript "I"). For system (2.2), the function $\mathcal{H}(U_F, U_I)$ is

$$\mathcal{H}(U_E, U_I) = \begin{pmatrix} -\nabla \cdot \mathbf{q}_I \\ -\nabla \cdot \left(\frac{\mathbf{q}_E \otimes \mathbf{q}_E}{\rho_E} \right) + \frac{1}{\varepsilon^2} p'(\rho_E) \nabla \rho_I \end{pmatrix}, \tag{3.26}$$

with $U_E = (\rho_E, \mathbf{q}_E)$ and $U_I = (\rho_I, \mathbf{q}_I)$. Then, the algorithm for the semi-implicit (SI) IMEX R-K schemes from t^n to t^{n+1} can be conveniently written as follows.

For i = 1 to s.

• Compute the internal stages:

$$U_E^{(i)} = U^n + \Delta t \sum_{i=1}^{i-1} \tilde{a}_{ij} \mathcal{H}(U_E^{(j)}, U_I^{(j)}), \quad U_*^{(i)} = U^n + \Delta t \sum_{i=1}^{i-1} a_{ij} \mathcal{H}(U_E^{(j)}, U_I^{(j)}).$$
(3.27)

• Solve for $U_I^{(i)}$

$$U_I^{(i)} = U_*^{(i)} + \Delta t a_{ii} \mathcal{H}(U_E^{(i)}, U_I^{(i)}). \tag{3.28}$$

That is, in component-wise, we have

$$\rho_I^{(i)} = \rho_I^* - \Delta t a_{ii} \nabla \cdot \mathbf{q}_I^{(i)},$$

$$\mathbf{q}_I^{(i)} = \mathbf{q}_I^* - \Delta t a_{ii} \frac{1}{\varepsilon^2} p'(\rho_E^{(i)}) \nabla \rho_I^{(i)},$$
(3.29)

with the known explicit quantities given from (3.27)

$$\rho_I^* = \rho^n - \Delta t \sum_{j=1}^{i-1} a_{ij} \nabla \cdot \mathbf{q}_I^{(j)},$$

$$\mathbf{q}_I^* = \mathbf{q}^n - \Delta t \sum_{j=1}^{i-1} a_{ij} \left(\nabla \cdot \left(\frac{\mathbf{q}_E \otimes \mathbf{q}_E}{\rho_E} \right)^{(j)} + p'(\rho_E^{(j)}) \nabla \rho_I^{(j)} \right).$$

Then from (3.29) substituting $\mathbf{q}_I^{(i)}$ into $\rho_I^{(i)}$, we get a linear system for $\rho_I^{(i)}$, i.e.

$$\rho_I^{(i)} = \rho_I^{**} + \Delta t^2 a_{ii}^2 \frac{1}{\varepsilon^2} \nabla \cdot \left(p'(\rho_E^{(i)}) \nabla \rho_I^{(i)} \right),$$

with

$$\rho_I^{**} = \rho_I^* - \Delta t a_{ii} \nabla \cdot \mathbf{q}_I^*$$

After solving $\rho_I^{(i)}$, we compute $\mathbf{q}_I^{(i)}$ from the second equation in (3.29). Finally, update the numerical solution:

$$U^{n+1} = U^n + \Delta t \sum_{i=1}^{s} b_i \mathcal{H}(U_E^i, U_I^i). \tag{3.30}$$

Remark 3.2. This approach takes the advantage of linearization by avoiding solving nonlinear systems, yet it maintains the high order accuracy of the IMEX scheme. U^{n+1} is finally updated by the implicit part of the Butcher tableau using weights b^T . The assumption that the implicit part of the Butcher tableau is stiffly accurate, is crucial, for asymptotic consistency and accuracy of the scheme, as shown in the Appendix A.

Remark 3.3. In the next section, we perform AP analysis for NI IMEX-RK, which suggests the use of IMEX schemes with globally stiffly accurate (GSA) property; in the Appendix A, we perform similar analysis for the SI IMEX-RK approach, which suggests the use of IMEX schemes with stiffly accurate (SA) property. For definitions of GSA and SA, please see the next section. In our simulations, we carry out computations using these two approaches. It is shown that both of them are high order accurate and effective for problems with a wide range of Mach number.

3.4. High order spatial discretization

We now discuss high order extensions in space discretization. For nonlinear convection terms, we apply high order shock-capturing schemes with the WENO reconstruction; and for second order derivative terms, we adopt high order central difference. In particular, we apply the following procedure to discretize spatial gradients in equation (3.12) in the 1D first order IMEX-RK case. Extensions to multi-dimensional cases can be done in a dimension-by-dimension fashion, thanks to the framework of finite difference schemes [14]; while extensions to high order IMEX-RK schemes can be done in a stage-by-stage manner as discussed above. We make sure that the approximation to spatial derivatives are in a flux-difference form, so that conservation of mass and momentum are guaranteed. We also notice that all these spatial derivatives are discretized in an "explicit" way, except for the term Δp^{n+1} . For these explicit treatments, a nonlinear WENO type reconstruction can be applied if needed; while for the implicit treatment of the Laplace operator on p, a linear fourth order finite difference scheme is used.

1. $\nabla \cdot \mathbf{q}^n$ and $\nabla \cdot (\mathbf{q} \otimes \mathbf{q}/\rho)^n$ in equation (3.12): A local Lax-Friedrichs type flux splitting, with numerical viscosity proportional to the flow velocity, can be applied with various reconstruction techniques, such as the second order total variation diminishing (TVD), the third order total variation bounded (TVB), and the fifth order WENO reconstruction [36].

Flux derivative $\partial_x q|_{x_j}$ can be approximated by $\frac{1}{\Delta x}(\hat{q}_{j+1/2}-\hat{q}_{j-1/2})$, with numerical fluxes $\hat{q}_{j+\frac{1}{2}}=\hat{q}_{j+\frac{1}{2}}^++\hat{q}_{j+\frac{1}{2}}^-$. In a finite difference setting, $\hat{q}_{j+\frac{1}{2}}^-$ is reconstructed in a upwind fashion (with left-biased stencil) from $\{q_l^+\}$, $l=j-k,\cdots j+k$ at neighboring grid points with $q_l^+=\frac{1}{2}(q_l+\alpha\rho_l)$; while $\hat{q}_{j+\frac{1}{2}}^+$ is reconstructed in an upwind fashion (with right-biased stencil) from $\{q_l^-\}$, $l=j-k+1,\cdots j+k+1$ at neighboring grid points with $q_l^-=\frac{1}{2}(q_l-\alpha\rho_l)$. k depends on the order of reconstruction, e.g. for a first order scheme k=0, for a second order TVD or third order TVB scheme k=1 and for a fifth order WENO scheme k=2. Here α , as a parameter in the Lax-Friedrichs flux, is chosen as

$$\max_{u}\{|u|\} + \min(1, 1/\varepsilon)\sqrt{p'(\rho)}.$$

It is independent of the Mach number ε . Details of such reconstruction procedures can be found in [14]. Other first order derivatives can be approximated in a similar manner, thus the details are skipped.

- 2. $\frac{1}{\varepsilon^2}\nabla p(\rho^{n+1})$ in equation (3.12): Notice that this term is approximated in an "explicit" manner, as p^{n+1} is explicitly known from an implicit solver from the first sub-equation of (3.12). A local Lax-Friedrichs type flux splitting, with zero numerical viscosity can be applied with non-oscillatory reconstruction techniques. The nonlinear reconstruction procedure is the same as that for the first order derivative terms just discussed; the difference is that we use zero viscosity here. With $p^{n+1} = p_0^{n+1} + \varepsilon^2 p_2^{n+1} + \cdots$, we notice that in the zero limit of Mach number, p_0^{n+1} is constant (from an implicit treatment) and $\frac{1}{\varepsilon^2}\nabla p(\rho^{n+1})$ is effectively a non-stiff term ∇p_2^{n+1} . Zero numerical viscosity is essential, otherwise the numerical diffusion will become large (proportional to $\frac{1}{\varepsilon^2}$) when $\varepsilon \to 0$.
- 3. Δp . For example p_{xx} can be approximated by a standard fourth order scheme:

$$p_{xx}|_{x_j} = \frac{-p_{j-2} + 16p_{j-1} - 30p_j + 16p_{j+1} - p_{j+2}}{12\Delta x^2} + \mathcal{O}(\Delta x^4).$$

Similar formula can be applied to the second derivative terms in the form of p_{yy} .

4. $\nabla^2: \left(\frac{\mathbf{q} \otimes \mathbf{q}}{\rho}\right)$. The second derivative terms in the form of u_{xx} or u_{yy} can be approximated in the same way as above, while the mixed derivative term in the form of u_{xy} can be approximated dimension by dimension, by a fourth order central difference scheme, e.g.

$$u_{x|x_{j}} = \frac{u_{j-2} - 8u_{j-1} + 8u_{j+1} - u_{j+2}}{12\Delta x^{2}} + \mathcal{O}(\Delta x^{4})$$

5. To avoid solving the nonlinear system, we propose to linearize $p(\rho^{n+1})$ in equation (3.12), by discretizing $\partial_x(p'(\rho^n)\partial_x\rho^{n+1})$ with high order in space. A prototype problem is to discretize $(a(x)u_x)_x$ with high order. For example, it can be checked by local truncation error analysis that the following formula provides a fourth order approximation to $(a(x)u_x)_x$, with a five-point stencil

$$(a(x)u_x)_{x|x_j} = \frac{1}{\Delta x^2}(a_{j-2}, a_{j-1}, a_j, a_{j+1}, a_{j+2})$$

$$\begin{pmatrix}
-25/144 & 1/3 & -1/4 & 1/9 & -1/48 \\
1/6 & 5/9 & -1 & 1/3 & -1/18 \\
0 & 0 & 0 & 0 & 0 \\
-1/18 & 1/3 & -1 & 5/9 & 1/6 \\
-1/48 & 1/9 & -1/4 & 1/3 & -25/144
\end{pmatrix}\begin{pmatrix}
u_{j-2} \\
u_{j-1} \\
u_j \\
u_{j+1} \\
u_{j+2}
\end{pmatrix} + \mathcal{O}(\Delta x^4).$$

This is the formula that we used in our high order implementation.

4. AP property

In this section we recognize that GSA [10] and SA [26] are important properties for NI IMEX-RK and SI IMEX-RK approaches respectively, in order to guarantee the asymptotic preserving property as $\varepsilon \to 0$.

Let's first recall the definition of GSA.

Definition 4.1. An IMEX-RK scheme is GSA if it satisfies the following

$$b^T = e_s^T A$$
, $\tilde{b}^T = e_s^T \tilde{A}$,

with $e_s = (0, ..., 0, 1)^T$, and $c_s = \tilde{c}_s = 1$.

Roughly speaking GSA means that the numerical solution of an IMEX RK method coincides with the last stage of the scheme. Next, we will prove that, GSA is a sufficient assumption to guarantee the asymptotic consistency and accuracy, in the limit of zero Mach number.

Proposition 4.2. Consider applying an IMEX-RK scheme, of order p with the matrix A for the implicit scheme in the double Butcher tableau invertible, to system (2.2) in a bounded domain $\Omega \in \mathbb{R}^d$, with zero Neumann condition. Assume that the IMEX-RK method is GSA. Assume the well-prepared initial conditions (2.8) with ρ_0^0 being constant and $\nabla_{\mathbf{x}} \cdot \mathbf{u}_0^0(\mathbf{x}) = 0$. Let us denote by $(\rho^1(\mathbf{x}; \varepsilon))$, $\mathbf{u}^1(\mathbf{x}; \varepsilon)$) the numerical solution after one step. Then we have:

$$\lim_{\varepsilon \to 0} \rho^{1}(\mathbf{x}; \varepsilon) = \rho_{0}^{0}, \quad \lim_{\varepsilon \to 0} \nabla_{\mathbf{x}} \cdot \mathbf{u}^{1}(\mathbf{x}; \varepsilon) = 0. \tag{4.31}$$

Furthermore, let $\mathbf{u}_{inc}(\mathbf{x},t)$ be the exact solution of the incompressible Euler equations with initial data $\mathbf{u}_{inc}(\mathbf{x},0) = \mathbf{u}_0^0(\mathbf{x})$. Then one has the following one-step error estimate

$$\lim_{\varepsilon \to 0} \mathbf{u}^{1}(\mathbf{x}; \varepsilon) = \mathbf{u}_{inc}(\mathbf{x}, \Delta t) + \mathcal{O}(\Delta t^{p+1}). \tag{4.32}$$

Proof. We apply an IMEX-RK scheme with double Butcher tableau eq. (3.20) to system (2.2a)-(2.2b), and get the following IMEX-RK solutions in a vectorial form

$$\rho^{1} = \rho^{0} - \Delta t \underline{b}^{T} \nabla_{\mathbf{x}} \cdot \underline{\mathbf{q}},$$

$$\mathbf{q}^{1} = \mathbf{q}^{0} - \Delta t \underline{\tilde{b}}^{T} \nabla_{\mathbf{x}} \cdot \underline{\mathbf{f}} - \frac{\Delta t}{\varepsilon^{2}} \underline{b}^{T} \nabla_{\mathbf{x}} \underline{p},$$

$$(4.33)$$

where ρ^1 and \mathbf{q}^1 are numerical solutions after one time step, and

$$\underline{\rho} = \rho^{0} \underline{e} - \Delta t A \nabla_{\mathbf{x}} \cdot \underline{\mathbf{q}},$$

$$\underline{\mathbf{q}} = \mathbf{q}^{0} \underline{e} - \Delta t \tilde{A} \nabla_{\mathbf{x}} \cdot \underline{\mathbf{f}} - \frac{\Delta t}{c^{2}} A \nabla_{\mathbf{x}} \underline{p},$$
(4.34)

where $\mathbf{f} := \mathbf{q} \otimes \mathbf{q}/\rho$, $\underline{e} = (1, \dots, 1)^T$. Here, $\underline{\cdot}$ indicates a vector, whose components corresponding to IMEX-RK intermediate stages. For example, $\underline{\rho} = (\rho_1, \dots \rho_s)$ are numerical approximations of ρ at IMEX-RK intermediate stages $t_i = t^0 + c_i \Delta t$ for $i = 1, \dots s$; let $\mathbf{q} = (q_1, \dots q_d)^T$ and $\underline{\mathbf{q}} = (\mathbf{q}_1, \dots, \mathbf{q}_s)$ with $\mathbf{q}_i \approx \mathbf{q}(\mathbf{x}, t_i)$ are numerical solutions of \mathbf{q} at IMEX-RK intermediate stages. Similar notations are used for other variables.

In system (4.34), inserting **q** into the equation for ρ , we get

$$\frac{\Delta t^2}{\varepsilon^2} A^2 \Delta \underline{p} = (\underline{\rho} - \rho^0 \underline{e}) + \Delta t A \nabla_{\mathbf{x}} \cdot \mathbf{q}^0 \underline{e} - \Delta t^2 A \tilde{A} \nabla_{\mathbf{x}}^2 : \underline{\mathbf{f}}. \tag{4.35}$$

Note that A is of size $s \times s$, while **x** and $\nabla_{\mathbf{x}}$ is of size $d \times 1$.

Now we consider the following formal ε -asymptotic expansion of stage-value vectorial quantities $\underline{\rho}$, $\underline{\mathbf{q}}$, \underline{p} and of the numerical solutions ρ^1 , \mathbf{q}^1 , p^1 ,

$$\underline{\rho}(\mathbf{x}) = \underline{\rho}_0(\mathbf{x}) + \varepsilon^2 \underline{\rho}_2(\mathbf{x}) + \cdots, \qquad \rho^1(\mathbf{x}) = \rho_0^1 + \varepsilon^2 \rho_2^1(\mathbf{x}) + \cdots,
\underline{\mathbf{q}}(\mathbf{x}) = \underline{\mathbf{q}}_0(\mathbf{x}) + \mathcal{O}(\varepsilon^2), \qquad \qquad \mathbf{q}^1(\mathbf{x}) = \mathbf{q}_0^1(\mathbf{x}) + \mathcal{O}(\varepsilon^2),
\underline{p} := \underline{p}_0(\mathbf{x}) + \varepsilon^2 \underline{p}_2(\mathbf{x}) + \cdots, \qquad p^1 = p_0^1 + \varepsilon^2 p_2^1(\mathbf{x}) + \cdots.$$
(4.36)

Asymptotic consistency for solutions at IMEX-RK intermediate stages. Plugging (4.36) into (4.34), we get for the $\mathcal{O}(\varepsilon^{-2})$ term:

$$\nabla_{\mathbf{x}} p_0 := \nabla_{\mathbf{x}} p(\rho_0) = 0,$$

which implies that \underline{p}_0 and $\underline{\rho}_0$ are independent of space; and get for $\mathcal{O}(1)$ terms in ε :

$$\frac{\underline{\rho}_0 - \rho_0^0 \underline{e}}{\Delta t} = -A \nabla_{\mathbf{x}} \cdot \underline{\mathbf{q}}_0, \tag{4.37}$$

and

$$\mathbf{q}_{0} = \mathbf{q}_{0}^{0} \underline{e} - \Delta t \tilde{A} \nabla_{\mathbf{x}} \cdot \underline{\mathbf{f}}_{0} - \Delta t A \nabla_{\mathbf{x}} p_{2}. \tag{4.38}$$

Integrating (4.37) over the computational domain Ω and by considering the boundary conditions, one gets

$$\underline{\rho}_0 = \rho_0^0 \underline{e},\tag{4.39}$$

that is ρ_0 is also independent of time. Now, by (4.35) and invertibility of matrix A, the $\mathcal{O}(1)$ term in ε is:

$$\Delta t^2 \Delta \underline{p}_2 = A^{-2} (\underline{\rho}_0 - \rho_0^0 \underline{e}) + \Delta t A^{-1} \nabla_{\mathbf{x}} \cdot \mathbf{q}_0^0 \underline{e} - \Delta t^2 A^{-1} \tilde{A} \nabla_{\mathbf{x}}^2 : \underline{\mathbf{f}}_0. \tag{4.40}$$

By (4.39) and the hypothesis: $\nabla_{\mathbf{x}} \cdot \mathbf{q}_0^0 = \rho_0^0 \nabla_{\mathbf{x}} \cdot \mathbf{u}_0^0 = 0$, then (4.40) is reduced to:

$$\Delta p_2 = -A^{-1}\tilde{A}\nabla_{\mathbf{x}}^2 : \underline{\mathbf{f}}_0. \tag{4.41}$$

Now by taking the divergence of \mathbf{q}_0 in (4.38) and by $\nabla_{\mathbf{x}} \cdot \mathbf{q}_0^0 = \rho_0^0 \nabla_{\mathbf{x}} \cdot \mathbf{u}_0^0 = 0$ for hypothesis, we get:

$$\nabla_{\mathbf{x}} \cdot \mathbf{q}_0 = -\Delta t \tilde{A} \nabla_{\mathbf{x}}^2 : \underline{\mathbf{f}}_0 - \Delta t A \Delta p_2 = 0, \tag{4.42}$$

then

$$\nabla_{\mathbf{x}} \cdot \underline{\mathbf{u}}_0 = 0. \tag{4.43}$$

Asymptotic consistency for ρ^1 and \mathbf{q}^1 . In (4.33), the $\mathcal{O}(1)$ term of the density equation is

$$\rho_0^1 = \rho_0^0 - \Delta t b^T \nabla_{\mathbf{X}} \cdot \mathbf{q}_0, \tag{4.44}$$

and by (4.42) one gets: $\rho_0^1 = \rho_0^0$, i.e. $\rho^1(\mathbf{x}; \varepsilon) \to \rho_0^0$ for $\varepsilon \to 0$. Now from (4.33), we take into account the $\mathcal{O}(1)$ term in ε :

$$\mathbf{q}_{0}^{1} = \mathbf{q}_{0}^{0} - \Delta t \underline{\tilde{b}}^{T} \nabla_{\mathbf{x}} \cdot \underline{\mathbf{f}}_{0} - \Delta t \underline{b}^{T} \nabla_{\mathbf{x}} p_{2}, \tag{4.45}$$

and taking the divergence, and inserting equation (4.41), we obtain

$$\nabla_{\mathbf{X}} \cdot \mathbf{q}_0^1 = \nabla_{\mathbf{X}} \cdot \mathbf{q}_0^0 - \Delta t (b^T A^{-1} \tilde{A} - \tilde{b}^T) \nabla_{\mathbf{X}}^2 : \underline{\mathbf{f}}_0.$$

By $\nabla_{\mathbf{x}} \cdot \mathbf{q}_0^0 = \rho_0^0 \nabla_{\mathbf{x}} \cdot \mathbf{u}_0^0 = 0$ and by the fact that the method is GSA (see Definition 4.1), i.e.

$$b^T A^{-1} \tilde{A} - \tilde{b}^T = e_s^T \tilde{A} - \tilde{b}^T = 0,$$

it follows:

$$\nabla_{\mathbf{x}} \cdot \mathbf{q}_0^1 = \rho_0^1 \nabla_{\mathbf{x}} \cdot \mathbf{u}_0^1 = \rho_0^0 \nabla_{\mathbf{x}} \cdot \mathbf{u}_0^1 = 0,$$

i.e., $\nabla_{\mathbf{x}} \cdot \mathbf{u}^1(\mathbf{x}; \varepsilon) \to 0$ for $\varepsilon \to 0$. Finally, we prove the asymptotic accuracy (4.32). In fact, by (4.45) and (4.38) with ρ_0^0 constant we get

$$\underline{\mathbf{u}}_{0} = \mathbf{u}_{0}^{0} - \Delta t \tilde{A} \frac{1}{\rho_{0}^{0}} \nabla_{\mathbf{x}} \cdot \underline{\mathbf{f}}_{0} - \Delta t A \frac{1}{\rho_{0}^{0}} \nabla_{\mathbf{x}} \underline{p}_{2},
\underline{\mathbf{u}}_{0}^{1} = \underline{\mathbf{u}}_{0}^{0} - \Delta t \tilde{b}^{T} \frac{1}{\rho_{0}^{0}} \nabla_{\mathbf{x}} \cdot \underline{\mathbf{f}}_{0} - \Delta t b^{T} \frac{1}{\rho_{0}^{0}} \nabla_{\mathbf{x}} \underline{p}_{2}, \tag{4.46}$$

which represents the time discretization of eq. (2.6) by the IMEX scheme of classical order p, with

$$\Delta \underline{p}_2 = -A^{-1}\tilde{A}\nabla_{\mathbf{x}}^2 : \underline{\mathbf{f}}_0.$$

Then if $\mathbf{u}_{inc}(\mathbf{x}, \mathbf{t})$ is the exact solution of eq. (2.6) with initial data $\mathbf{u}_{inc}(\mathbf{x}, 0) = \mathbf{u}_0^0$. From (4.46), one gets the asymptotic accuracy, i.e. the eq. (4.32).

Note that similarly consideration can be built for periodic boundary conditions or open boundary with a zero boundary condition at infinity [25].

Remark 4.3. We make the assumption that the *A* matrix for the implicit scheme in the double Butcher tableau is invertible, that is the IMEX method is of type A. The same conclusion can be drawn for the IMEX-RK methods that are of type CK or of type ARS. The proof follows similar lines of argument, thus is omitted to save space. For definitions of type A, CK and ARS, please see [3]. The asymptotic analysis above is performed for semi-discrete schemes, i.e. the spatial derivatives are assumed to be continuous. The analysis for a fully discrete scheme can be performed, yet the algebra will be much more involved. We omit to present them to save space.

Remark 4.4. If we consider the semi-implicit linearized treatment, we do not require the GSA assumption, but only the SA assumption. We give a brief sketch of the result in the Appendix A.

5. Numerical results for isentropic gas dynamics

In this section, we perform extensive numerical tests for the proposed approaches: NI IMEX-RK and SI IMEX-RK. For NI IMEX-RK approach, we solve the nonlinear elliptic equation for the pressure p with a Newton solver, while for the SI IMEX-RK approach, we perform a linearization with the high order IMEX framework discussed in Section 3.3. We test our new schemes by several 1D and 2D test cases, and with different values of the Mach number ε ranging from compressible to incompressible regimes. For all numerical tests, we provide well prepared initial conditions, unless otherwise indicated.

5.1. 1D numerical tests

Example 5.1. (Convergence test on a simple wave problem.) We first verify the order of convergence of the two IMEX RK approaches. We consider the following test for the isentropic Euler equations with $p = \rho^2$ on a computational domain of [0, 1] with initial data:

$$u_0 = \sin(2\pi x), \quad \rho_0 = \left(\frac{\varepsilon(\gamma - 1)}{2\sqrt{\gamma}}(u + 1.1)\right)^{2/(\gamma - 1)}, \quad p_0 = \rho_0^2.$$

We measure the errors by a comparison with the exact solution, which is computed on the grid by the method of characteristics and Newton's iteration with tolerance 10^{-12} . In Tables 5.1–5.2, we show the L^1 errors and the corresponding orders of convergence in time for the density for a second and a third order IMEX method, respectively with Butcher tableaux (B.2) and (B.6) provided in the Appendix B. We observe the expected order of accuracy in time. We also perform numerical tests using other second and third order IMEX methods with Butcher tableaux (B.3) and (B.4). As in the previous case, the expected order of convergence is observed. We omit to present those tables in order to save space.

Example 5.2. (Riemann problem from Degond-Tang [19].) We consider the following initial data

$$\begin{cases} \rho(x,0) = 1, & q(x,0) = 1 - \varepsilon^2/2, & x \in [0,0.2] \bigcup [0.8,1], \\ \rho(x,0) = 1 + \varepsilon^2, & q(x,0) = 1, & x \in (0.2,0.3], \\ \rho(x,0) = 1, & q(x,0) = 1 + \varepsilon^2/2, & x \in (0.3,0.7], \\ \rho(x,0) = 1 - \varepsilon^2, & q(x,0) = 1, & x \in (0.7,0.8]. \end{cases}$$
(5.47)

This example consists of several Riemann problems. We let $p(\rho) = \rho^2$ and assume periodic boundary conditions. We choose $\varepsilon = 0.8, 0.3, 0.05$ and present the corresponding results in Fig. 5.2. We note that when ε is relatively large, shocks and contact discontinuities appear. When ε is small the solutions are almost constants.

In Fig. 5.2, we compare performances of first, second and third order schemes. Please see the caption of the figure, for more descriptions of these schemes. It is observed that, in general, schemes with higher order accuracy can better capture solutions. In the case when the Mach number is small $\varepsilon=0.05$ (which gives $\varepsilon^2=2.5\times 10^{-3}$) the scheme projects the solution to the incompressible limit solution faster than an explicit scheme. Our schemes manage to capture the macro-structure of the solution when ε becomes small, at reasonable cost and using an under-resolved mesh. Thanks to the TVD/TVB/WENO reconstructions, our schemes successfully capture solutions around regions with large gradients. The performance of SI-IMEX RK scheme is similar to those of IMEX RK scheme presented in Fig. 5.2. Thus we don't repeat the presentation to save space.

Example 5.3. (Two colliding acoustic waves.) We simulate the evolution of two colliding waves as in [19]. We consider non-well prepared initial conditions:

Table 5.1
Example 5.1. Second order SA SSP(3,3,2) with Butcher tableau (B.2).

N	NI IMEX-RK scheme									
	$\varepsilon = 1$		$\varepsilon = 0.1$		$\varepsilon = 0.0001$	$\varepsilon = 0.0001$				
	L ¹ error	L ¹ order	L ¹ error	L ¹ order	L ¹ error	L ¹ order				
40	3.58e-02	-	2.96e-02	_	2.91e-02	_				
80	1.59e-02	1.17	1.32e-02	1.17	1.30e-02	1.16				
160	5.40e-03	1.56	4.48e-03	1.56	4.54e-03	1.52				
320	1.50e-03	1.85	1.29e-03	1.80	1.30e-03	1.81				
640	3.94e-04	1.93	3.48e-04	1.89	3.40e-04	1.93				
1280	9.89e-05	2.00	8.81e-05	1.98	8.84e-05	1.94				

N	SI IMEX-RK scheme								
	$\frac{\varepsilon = 1}{L^1 \text{ error}}$ $L^1 \text{ order}$		$\varepsilon = 0.1$		$\varepsilon = 0.0001$				
			L^1 error L^1 order		L ¹ error	L ¹ order			
40	3.79e-02	_	3.03e-02	_	2.99e-02	_			
80	1.59e-02	1.26	1.29e-02	1.24	1.26e-02	1.25			
160	5.33e-03	1.58	4.35e-03	1.56	4.39e-03	1.52			
320	1.47e-03	1.86	1.24e-03	1.81	1.25e-03	1.81			
640	3.84e - 04	1.94	3.33e-04	1.90	3.28e-04	1.93			
1280	9.96e-05	1.95	8.70e-05	1.94	8.73e-05	1.91			

Table 5.2 Example 5.1. Third order GSA ARS(4,4,3) with Butcher tableau (B.6).

N	NI IMEX-RK scheme									
	$\varepsilon = 1$		$\varepsilon = 0.1$		$\varepsilon = 0.0001$					
	L ¹ error	L ¹ order	L ¹ error	L ¹ order	L ¹ error	L ¹ order				
120	9.48e-04	_	7.77e-04	_	7.64e-04	_				
240	1.24e-04	2.94	1.00e-04	2.95	9.87e-05	2.95				
480	1.55e-05	3.00	1.25e-05	3.00	1.24e-05	2.99				
960	1.94e-06	3.00	1.57e-06	3.00	1.57e-06	2.98				
N	SI IMEX-RK s	scheme								
			0.4		0.0004					

IN	SI IIVIEX-RK	scneme					
	$\frac{\varepsilon = 1}{L^1 \text{ error}} \qquad L^1 \text{ order}$		$\varepsilon = 0.1$		$\varepsilon = 0.0001$		
			L ¹ error	L ¹ order	L ¹ error	L ¹ order	
120	9.33e-04	-	7.05e-04	_	6.89e-04	_	
240	1.21e-04	2.94	8.95e-05	2.98	8.64e-05	2.99	
480	1.51e-05	3.00	1.11e-05	3.01	1.07e-05	3.01	
960	1.88e-06	3.00	1.38e-06	3.01	1.33e-06	3.01	

$$p(\rho) = \rho^{\gamma},$$

$$\rho(x, 0) = 0.955 + 0.5\varepsilon(1 - \cos(2\pi x)),$$

$$u(x, 0) = -\sin(x)\sqrt{\gamma}(1 - \cos(2\pi x)),$$

with $\gamma=1.4$, $x\in[-1,1]$ and $\varepsilon=0.1$. Periodic boundary conditions are considered. Note that *non-well prepared initial* conditions mean that when ε is small, the density and momentum are not close to the solutions of the incompressible Euler equations. In Fig. 5.3, we show the density and momentum at different times T. The solid line is the reference solution calculated with N=1000 and using the classical time step $\Delta t=0.5\Delta x/(\max(u)+c/\varepsilon)$. In this figure, the first, second and third order schemes are the same schemes used in Fig. 5.2.

Example 5.4. (1D Riemann problem.) We now consider 1D Riemann problems from [25], to show that in the compressible flow regime when the Mach number is $\mathcal{O}(1)$, our scheme also has good performances. We first take the initial data

$$\rho(x,0) = \begin{cases} 3, & x < 0.5, \\ 1, & x \ge 0.5, \end{cases} \qquad u(x,0) = 0, \tag{5.48}$$

with $\gamma=1.4$ on the domain $x\in[0,1]$. Reflective boundary conditions are considered and we take N=100. Here we choose a 3rd order SI IMEX RK scheme with Butcher tableau (B.5) in time, and 5th order finite difference WENO scheme in space. We show the results for $\varepsilon=1$ at T=0.16 and $\varepsilon=20$ at T=1.8 in Fig. 5.4. For both cases, the results match the exact solutions very well.

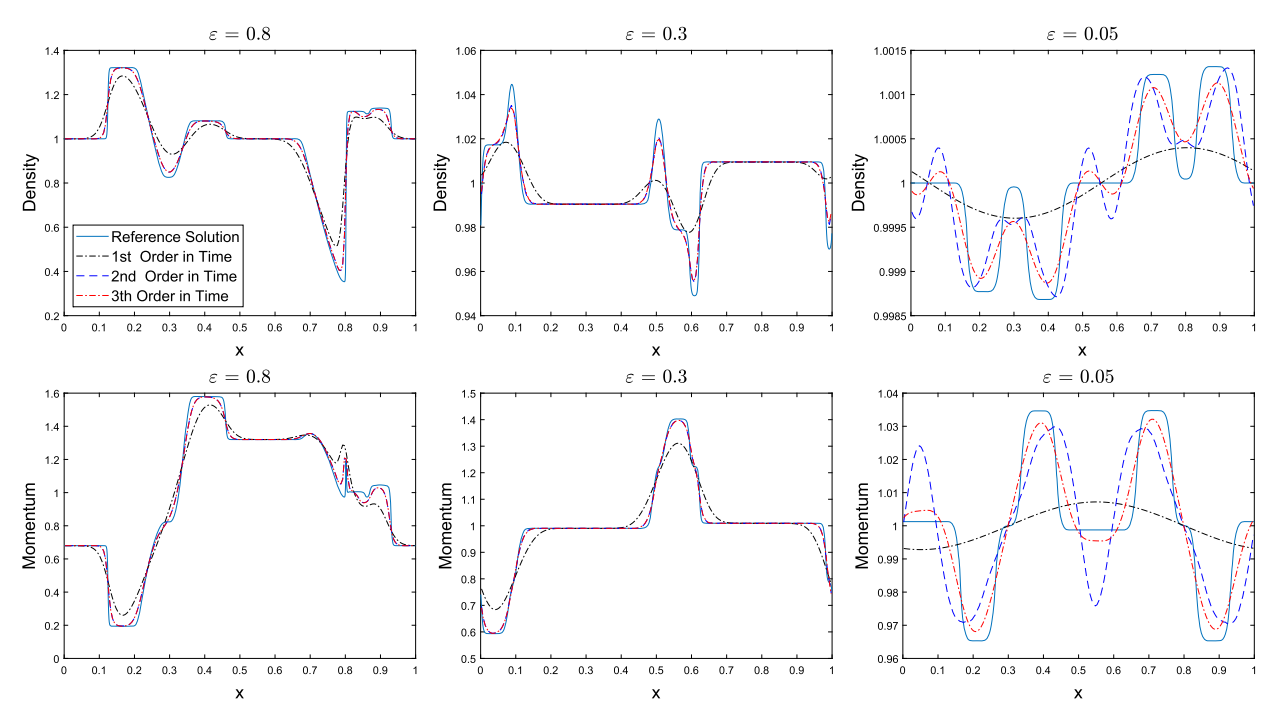


Fig. 5.2. Example 5.2. Numerical results of the Riemann problem at final time T=0.05 with $\Delta t=0.5\Delta x$, N=200, for the density (top) and momentum (bottom) for the isentropic Euler equations, when $\varepsilon=0.8$ (left), 0.3 (middle) and 0.05 (right). The reference solution (dotted line) calculated with N=1000 and the classical time step $\Delta t=0.5\Delta x/(\max(u)+c/\varepsilon)$. We have three different color lines: ". - ." (black) "- -" (blue),"· - ." (red), that represent respectively, solutions from first, second and third order schemes. The first order scheme uses a first order IMEX with Butcher tableau (B.1) coupled with a second order TVD spatial reconstruction (1st order in time); the second order scheme uses a second order IMEX with Butcher tableau (B.3) coupled with a third order TVB reconstruction (2nd order in time); the third order scheme uses a third order IMEX with Butcher tableau (B.6) coupled with a fifth order WENO spatial reconstruction (3rd order in time).

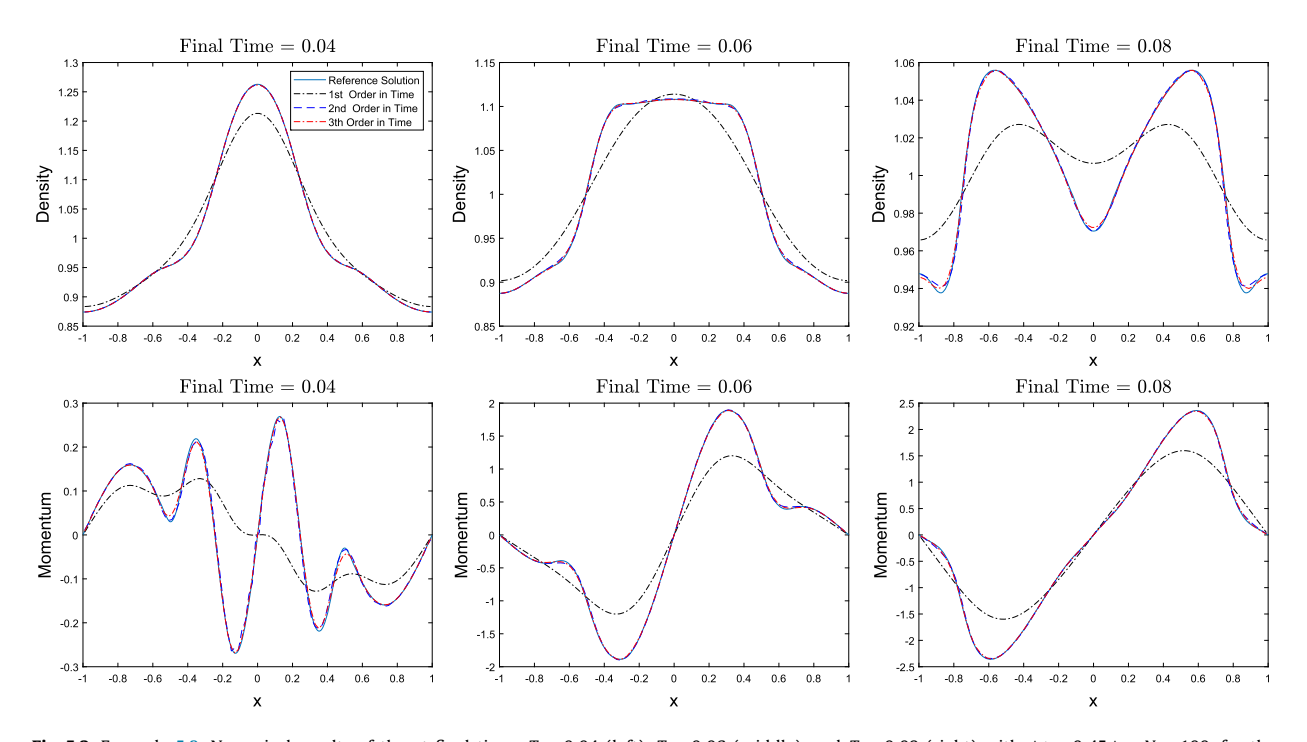


Fig. 5.3. Example 5.3. Numerical results of the at final times T=0.04 (left), T=0.06 (middle), and T=0.08 (right) with $\Delta t=0.45\Delta x$, N=100, for the density (top) and momentum (bottom) with $\varepsilon=0.1$. The solid line is the reference solution. We have three different color lines: " $\cdot - \cdot$ " (blue)," $\cdot - \cdot$ " (red), that represent respectively, solutions from first, second and third order schemes. These are the same schemes as those in Fig. 5.2.

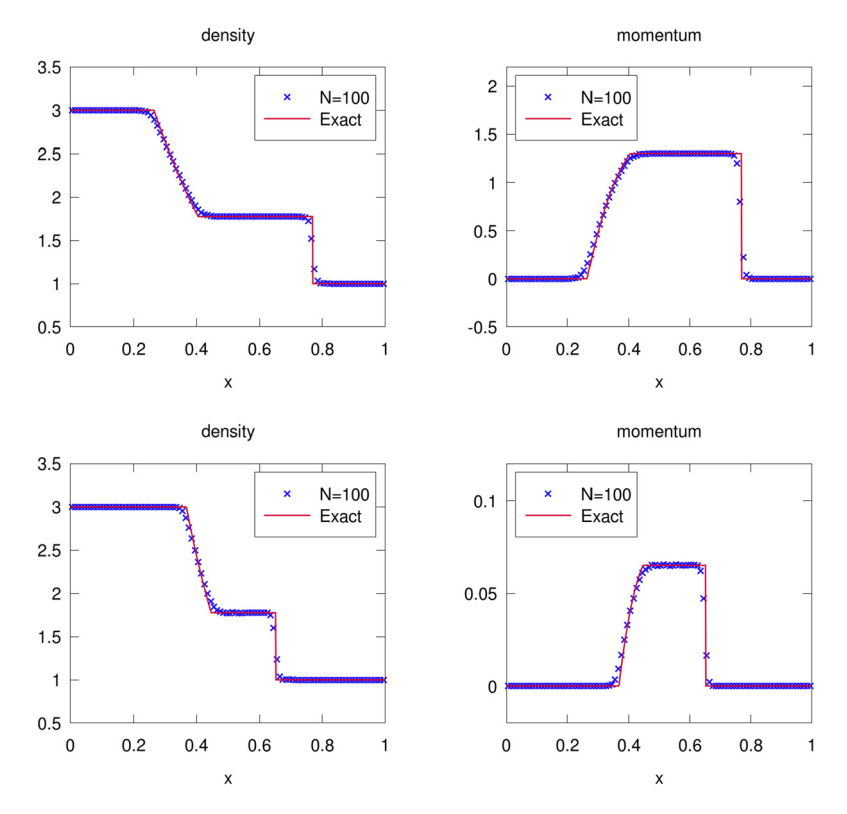


Fig. 5.4. Example 5.4 with initial data (5.48). 1D Riemann problem for $\varepsilon = 1$ at T = 0.16 (top) and for $\varepsilon = 20$ at T = 1.8 (bottom). Mesh grid: N = 100. The solid lines are the exact solutions.

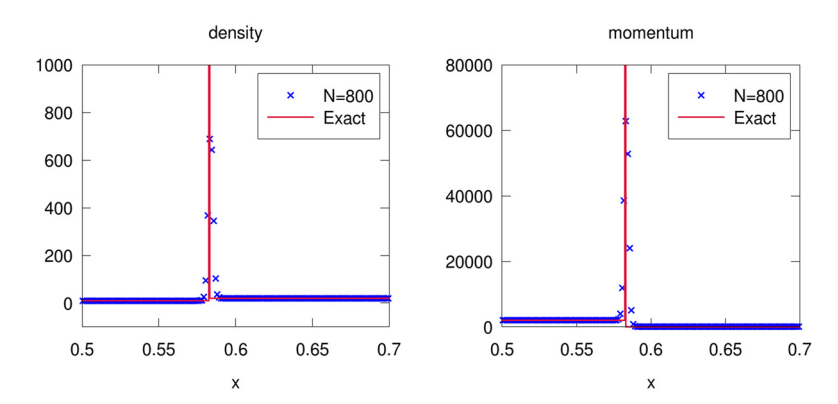


Fig. 5.5. Example 5.4 with initial data (5.49). 1D strong shock wave problem for $\varepsilon = 1$ at T = 0.001. Mesh grid: N = 800. The solid lines are the exact solutions.

Then we consider a 1D strong shock wave problem

$$\rho(x,0) = \begin{cases} 10, & x < 0.5, \\ 20, & x \ge 0.5, \end{cases} \qquad u(x,0) = \begin{cases} 2000, & x < 0.5, \\ 0, & x \ge 0.5, \end{cases}$$
 (5.49)

with $\gamma = 1.4$ on the domain $x \in [0, 1]$. Reflective boundary conditions are considered. Here we take N = 800. We show the results for $\varepsilon = 1$ at T = 0.001 in Fig. 5.5. Similarly, our numerical scheme can well capture the exact solution.

5.2. 2D numerical tests

For 2D numerical tests, we will only consider the SI IMEX-RK approach. We use a 3rd order SI IMEX-RK scheme with Butcher tableau (B.5) in time, and in space we take the 5th order finite difference WENO scheme. The mesh grid for the 2D problem is $N_x \times N_y$.

Table 5.3 Example 5.5. Convergence test for 2D isentropic Euler equations, $p = \rho^2$. T = 0.02. Semi-implicit IMEX RK approach. Errors are computed by comparing to a reference solution.

N	$\varepsilon = 1$		$\varepsilon = 0.1$		$\varepsilon = 0.01$		$\varepsilon = 0.0001$		
	L ¹ error	Order	L ¹ error	Order	L ¹ error	L ¹ error Order		Order	
8	1.19e-01	-	8.30e-03	-	2.74e-03	-	2.70e-03	_	
16	2.28e-02	2.38	8.04e - 04	3.37	1.11e-04	4.62	1.07e-04	4.66	
32	1.69e-03	3.76	1.01e-04	2.99	2.24e - 04	-	3.57e-06	4.91	
64	6.74e - 05	4.64	1.30e-05	2.96	2.89e - 04	-	1.20e-07	4.89	
128	2.21e-06	4.93	1.66e-06	2.97	4.00e-04	-	3.67e-09	5.03	

Example 5.5. (Convergence test.) We first verify orders of convergence in the 2D case. We take a computational domain $\Omega = [0, 1]^2$ with initial data:

$$\rho(x, y, 0) = 1 + \varepsilon^2 \sin^2(2\pi (x + y)),$$

$$\rho(x, y, 0) u(x, y, 0) = \sin(2\pi (x - y)) + \varepsilon^2 \sin(2\pi (x + y)),$$

$$\rho(x, y, 0) v(x, y, 0) = \sin(2\pi (x - y)) + \varepsilon^2 \cos(2\pi (x + y)).$$

and $p = \rho^2$. We choose $N_y = N_x$ and refine the mesh size by $N_x = 2^k \cdot N_{x,0}$, for k = 0, 1, 2, 3, with $N_{x,0} = 8$. The numerical errors are computed by comparing the numerical solutions of momentum q_1 on two consecutive mesh sizes. The final time is T = 0.02. In Table 5.3, we show the errors and orders for our scheme. Due to a small time step as compared to the spatial mesh size, for large $\varepsilon = 1$, we can observe 5th order spatial accuracy from mesh refinement. 5th order accuracy can also be clearly observed for very small $\varepsilon = 10^{-4}$. However, for intermediate values of ε , under the current mesh sizes, order degeneracy can be found, especially for $\varepsilon = 10^{-2}$. Such order reduction is a typical issue for high order IMEX RK methods [9] and is subject to our future investigation.

Example 5.6. (2D cylindrical explosion problem.) We now consider a 2D cylindrical explosion problem for the isentropic Euler system [21]. Here we take a nonlinear pressure-density relation $p = \rho^2$. The computational domain is set to be $\Omega = [-1, 1]^2$, with initial density given by

$$\rho(x, y, 0) = \begin{cases} 1 + \varepsilon^2 & \text{if } r^2 \le 1/4, \\ 1 & \text{else,} \end{cases}$$
 (5.50)

where $r = \sqrt{x^2 + y^2}$ is the distance from the cell center. The velocity field is set as

$$u = -\frac{\alpha(x, y)}{\rho(x, y, 0)} \frac{x}{r}, \quad v = -\frac{\alpha(x, y)}{\rho(x, y, 0)} \frac{y}{r},$$
 (5.51)

where the coefficient $\alpha(x, y)$ is given by $\alpha = \max(0, 1 - r)(1 - \exp(-16r^2))$ and we set u = 0, v = 0 if $r < 10^{-15}$. Periodic boundary conditions are considered and we use 100 grid points along each direction.

In Fig. 5.6, we show the surface of the density profile and the velocity field for $\varepsilon=1$ at different times T=0.1,0.24,0.3. In Fig. 5.7, we show the density profile, the velocity field and the discrete divergence error at time T=0.05 for a small value of $\varepsilon=10^{-3}$. In the latter case, the system is close to the incompressible limit, for which we can observe that the density is close to a constant, with deviation at the magnitude of 10^{-7} , i.e. in the order of $\mathcal{O}(\varepsilon^2)$. The divergence of the velocity field is around the magnitude of 10^{-5} . These plots indicate that our scheme can well capture the incompressible flow limit.

Example 5.7. (2D Riemann problem.) We consider a 2D Riemann problem for the isentropic Euler system [25]. We take $\gamma = 1.4$. The computational domain is set to be $\Omega = [-1, 1]^2$, with initial data as

$$\rho(x, y, 0) = \begin{cases} 0.5323 & x < 0.5, \ y \ge 0.5, & 1.5, & x \ge 0.5, \ y \ge 0.5, \\ 0.138 & x < 0.5, \ y < 0.5, & 0.5323, & x \ge 0.5, \ y < 0.5, \end{cases}$$

$$u(x, y, 0) = \begin{cases} 1.206 & x < 0.5, \ y \ge 0.5, & 0, & x \ge 0.5, \ y \ge 0.5, \\ 1.206 & x < 0.5, \ y < 0.5, & 0, & x \ge 0.5, \ y < 0.5, \end{cases}$$

$$v(x, y, 0) = \begin{cases} 0 & x < 0.5, \ y \ge 0.5, & 0, & x \ge 0.5, \ y < 0.5, \\ 1.206 & x < 0.5, \ y < 0.5, & 1.206, & x \ge 0.5, \ y < 0.5. \end{cases}$$

We consider a mesh grid of $N_x \times N_y = 200 \times 200$. In Fig. 5.8, we show the surface of the density profile for $\varepsilon = 1$ and $\varepsilon = 2$ at T = 0.1 respectively. From this test, we can see that our method can also obtain good results for $\varepsilon \ge 1$.

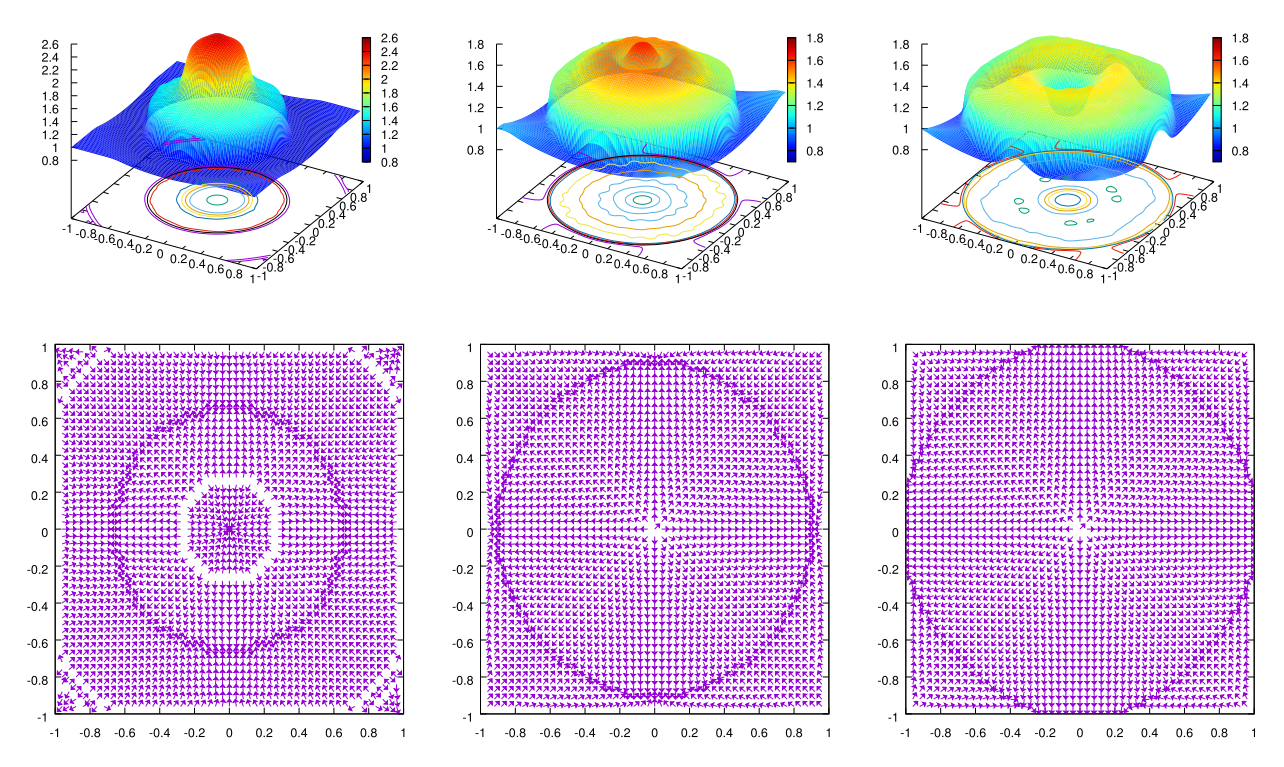


Fig. 5.6. Example 5.6. 2D cylindrical explosion problem for $\varepsilon = 1$ at T = 0.1 (left), T = 0.24 (middle) and T = 0.3 (right). Top images show the density profile; bottom images show the velocity field. Mesh grid: 100×100 .

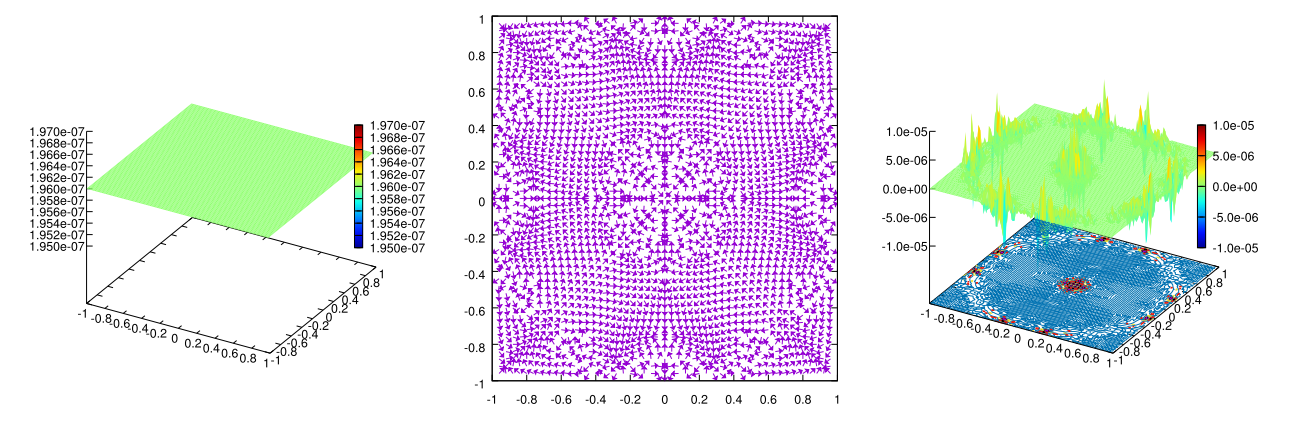


Fig. 5.7. Example 5.6. 2D cylindrical explosion problem for $\varepsilon = 10^{-3}$ at T = 0.05 for the deviation of density from 1 (left), the velocity field (middle) and divergence of the velocity field (right). Mesh grid: 100×100 .

Example 5.8. (Gresho vortex.) This is a time-dependent vortex which was first proposed by Gresho [23]. Following [35], initially a symmetric compact support vorticity distribution is centered at $(x_0, y_0) = (0.5, 0.5)$ with radius R = 0.4 in the domain $[0, 1]^2$. The initial background state is set as:

$$\rho_{\infty} = 1, \ \mathbf{u}_{\infty} = (u_{\infty}, 0), \ p_{\infty} = 1, \ c_{\infty} = \sqrt{\gamma \, p_{\infty} / \rho_{\infty}} = \sqrt{\gamma},$$

and the line velocity for the vortex is given by

$$u_{\theta}(r) = \begin{cases} 2r/R, & \text{if } 0 \le r < R/2, \\ 2(1 - r/R), & \text{if } R/2 \le r < R, \\ 0, & \text{if } r \ge R. \end{cases}$$
 (5.52)

The centrifugal force is balanced by the pressure gradient after scaled by ε^2 , that is

$$\rho_{\infty} \frac{u_{\theta}^2}{r} = \frac{1}{\varepsilon^2} \frac{\partial p_r}{\partial r},$$

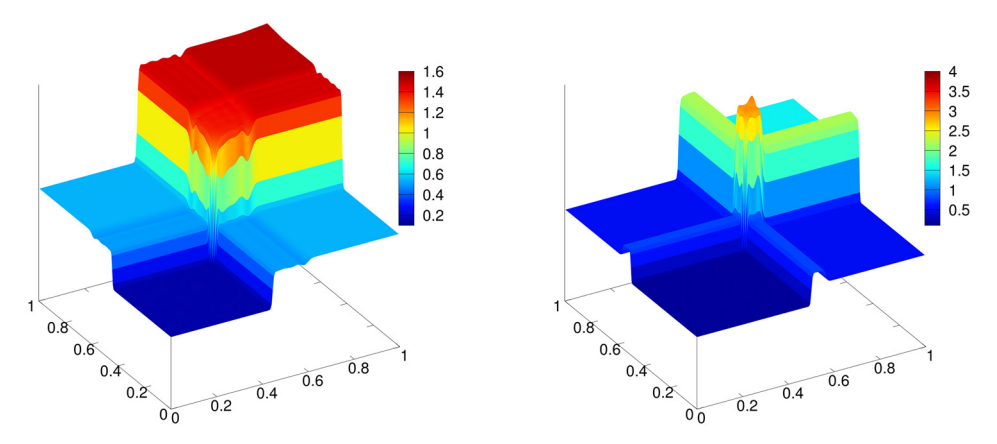


Fig. 5.8. Example 5.7. 2D Riemann problem at T=0.1 for $\varepsilon=1$ (left) and $\varepsilon=2$ (right). Mesh grid: 200×200 .

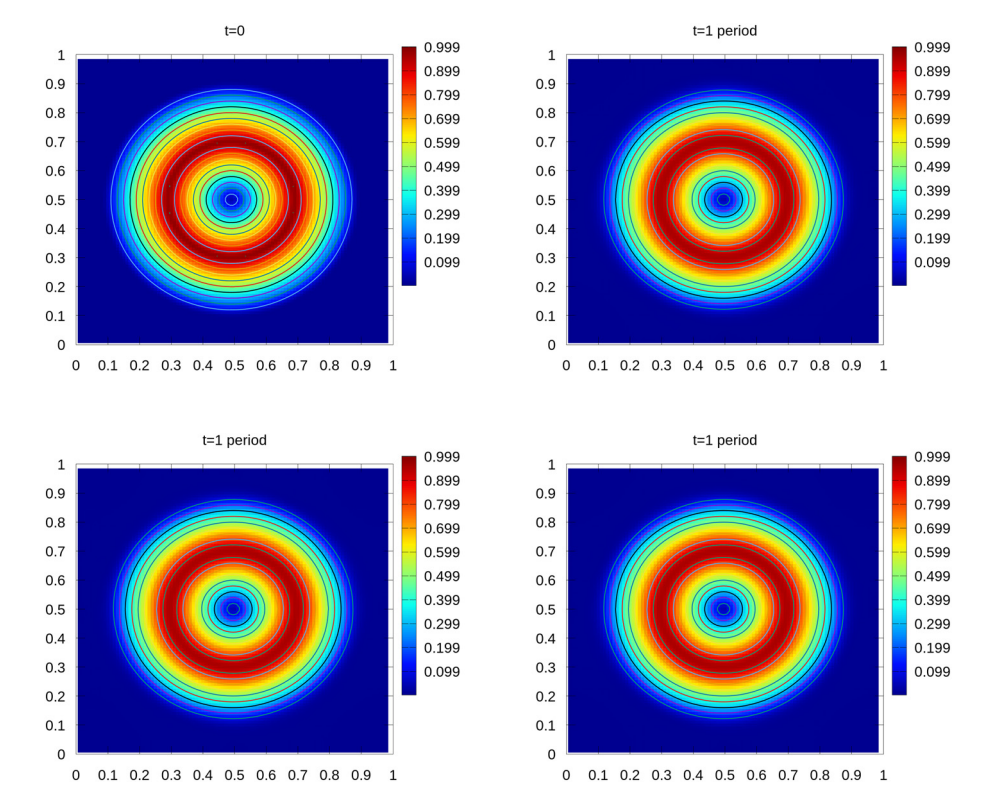


Fig. 5.9. Example 5.8, Gresho vortex problem. Top left: initial shape. Others are at $T = R\pi$ and shifted to the center by $-u_{\infty}t$ periodically, $\varepsilon = 0.1$ (top right), $\varepsilon = 0.01$ (bottom left), $\varepsilon = 0.001$ (bottom right). Mesh grid: 100×100 .

so the pressure is in the form of

$$p(r) = p_{\infty} + \varepsilon^{2} \begin{cases} 2(r/R)^{2} + 2 - \log 16, & \text{if } 0 \le r < R/2, \\ 2(r/R)^{2} - 4(2r/R + \log(r/R)) + 6, & \text{if } R/2 \le r < R, \\ 0, & \text{if } r \ge R, \end{cases}$$
(5.53)

where $r = \sqrt{(x-0.5)^2 + (y-0.5)^2}$. We assume adiabatic compression, i.e. $p = \rho^{\gamma}$ and we take $\gamma = 1.4$. For the velocity components, they are

$$u(x,y,0) = u_{\infty} - \frac{y - y_0}{r} u_{\theta}(r), \ v(x,y,0) = \frac{x - x_0}{r} u_{\theta}(r).$$

Notice that the such vorticity distribution produces a compactly supported velocity vector field.

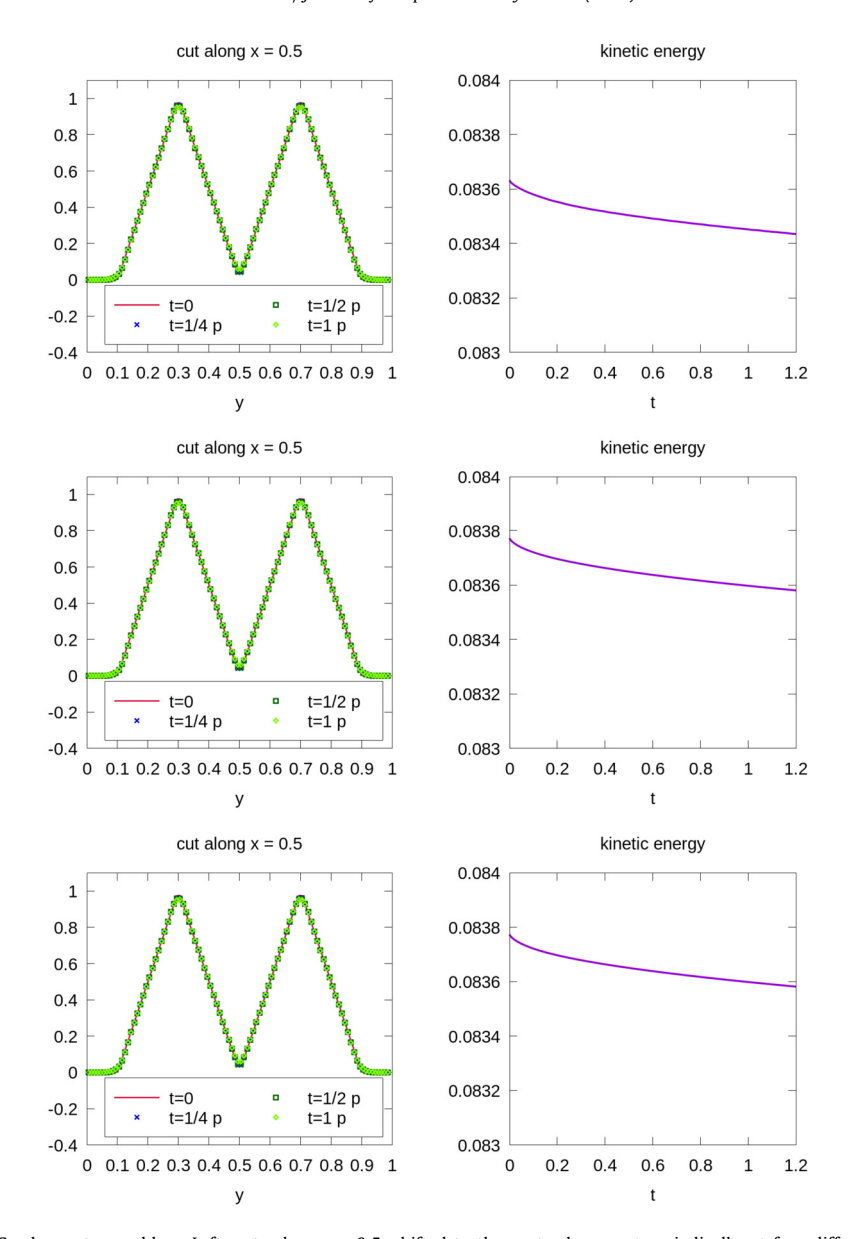


Fig. 5.10. Example 5.8, Gresho vortex problem. Left: cuts along x = 0.5, shifted to the center by $-u_{\infty}t$ periodically, at four different times, initial (t = 0), 1/4 period (t = 1/4p), 1/2 period (t = 1/2p) and 1 period (t = 1p). Right: time evolution of kinetic energy (5.54). From top to bottom: $\varepsilon = 0.1, 0.01, 0.001$. Mesh grid: 100×100 .

We consider periodic boundary conditions on both directions and use a mesh grid of $N_x \times N_y = 100 \times 100$. The background velocity is fixed with $u_\infty = 0.1$ moving in the *x*-direction, and we take $\varepsilon = 0.1, 0.01, 0.001$. For this problem, besides the transport velocity u_∞ , the line velocity for the rotating is u_θ and the corresponding angular velocity is u_θ/r , so the period for one rotating is $2\pi/(u_\theta/r) = R\pi$ if r < R/2. We use this time $T = R\pi$ as an approximate one rotating period. In Fig. 5.9, we show the isolines of the Mach number ratio, which is defined as

$$M_{\rm ratio} = \sqrt{[(u - u_{\infty})^2 + v^2]/(\gamma p/\rho)}.$$

We use 10 equally distributed contour lines within [0,1] starting from 0.099, and the vortex are shifted to the center by $-u_{\infty}t$ periodically. In Fig. 5.10 (left column), we show the cuts along x=0.5 at three different times, 1/4 period, 1/2 period and 1 full period, and compare them to the initial shape. We can see that the shapes of the vortex are well preserved for our high order scheme. In Fig. 5.10 (right column), we show the time evolution of averaged kinetic energy, which is defined

Table 5.4 Example 5.9. Accuracy test for the limit incompressible flow system when $\varepsilon = 0$.

N	16	32	64	128
L ¹ error	5.77e-03	2.23e-04	7.16e-06	2.07e-07
order	-	4.69	4.96	5.11

Table 5.5

Example 5.10. The L^1 errors and orders of the velocity u and L^∞ errors and orders of the divergence $u_x + v_y$ for the shear flow problem. The errors of u are computed by comparing to the reference solution computed by a spectral method. The divergence is computed by finite difference WENO reconstruction with zero viscosity.

	N	64	128	256
Velocity u	L^1 error order	2.91e-03 -	3.24e-04 3.17	1.61e-05 4.33
Divergence $u_x + v_y$	L^{∞} error order	1.02e-03	8.32e-05 3.87	8.29e-07 6.65

kinetic energy =
$$\sum_{i,j} \left[(u(x_i, y_j, t) - u_\infty)^2 + v(x_i, y_j, t)^2 \right] / N_x / N_y.$$
 (5.54)

We can see the conservation of kinetic energy is also well maintained, and essentially independent on ε .

5.3. Incompressible flow limit

Example 5.9. (Convergence test.) We consider the incompressible limit with $\varepsilon = 0$. Similarly we first test the accuracy of our scheme in this limit by taking initial conditions

$$u(x, y, 0) = -\sin(x)\sin(y), \quad v(x, y, 0) = \cos(x)\sin(y), \tag{5.55}$$

on the computational domain $[0, 2\pi]^2$. For this type of initial condition, we can easily verify that it has a stationary solution. We first take $\gamma = 1$ and run up to time T = 1 for the isentropic Euler equations. In Table 5.4, we show the L^1 errors and orders for the velocity u and we can clearly observe the 5th order spatial accuracy.

Example 5.10. Then we consider the shear flow problem on $[0, 2\pi]^2$ with

$$v(x, y, 0) = \delta \cos(x), \quad u(x, y, 0) = \begin{cases} \tanh((y - \pi/2)/\rho), & \text{if } y \le \pi \\ \tanh((3\pi/2 - y)/\rho), & \text{if } y > \pi. \end{cases}$$

We first compare the velocity u to a reference solution obtained by the spectral method solving the incompressible Euler equations in the vorticity stream function formulation [11]. We take $\varepsilon = 0$ and three mesh sizes N = 64, 128, 256, and run the solution to T = 1. The L^1 errors are shown in Table 5.5 and our results have good convergence to the reference solutions.

We also run the solution up to T=6 on a mesh grid 256×256 . The vorticity $\omega = v_x - u_y$ and the discrete divergence of velocity $u_x + v_y$ are shown in left and middle panels of Fig. 5.11. ω is obtained by the 4th order central difference. While for the divergence $u_x + v_y$, we mimic the flux reconstruction in the density equation in our scheme solving the isentropic Euler equations (note here the density is a constant), it is computed by finite difference WENO reconstruction with zero viscosity. We can observe that our scheme produces the vorticity similar to other high order schemes solving the incompressible Euler equations in the vorticity stream function formulation, e.g. [42]. The divergence of velocity is observed to be approximately in the order of $\mathcal{O}(h^3)$, where $h = \Delta x = \Delta y = 2\pi/256$. The corresponding time evolution of the L^{∞} norm of $u_x + v_y$ is plotted in the right panel of Fig. 5.11. We can see that the divergence increases, which is not surprising as the shear flow develops finer and finer scale structures with time evolution.

Example 5.11. Lastly we consider the Kelvin-Helmholtz instability problem [17,42] on $[0,4\pi] \times [0,2\pi]$ with

$$u(x, y, 0) = \cos(y), \quad v(x, y, 0) = 0.03 \sin(0.5x)$$

We run the solution up to T = 40 on the mesh grid $N_x \times N_y = 256 \times 128$. The vorticity $\omega = v_x - u_y$ and the discrete divergence of velocity $u_x + v_y$ are shown in the left and middle panels in Fig. 5.12, which are computed the same as the shear flow problem. We observe the vorticity is comparable to the results in [42]. This problem is a long time simulation, from Fig. 5.12 (right), we can see the divergence of the velocity also increases with time evolution, due to finer and finer scale structures appearing in the solution.

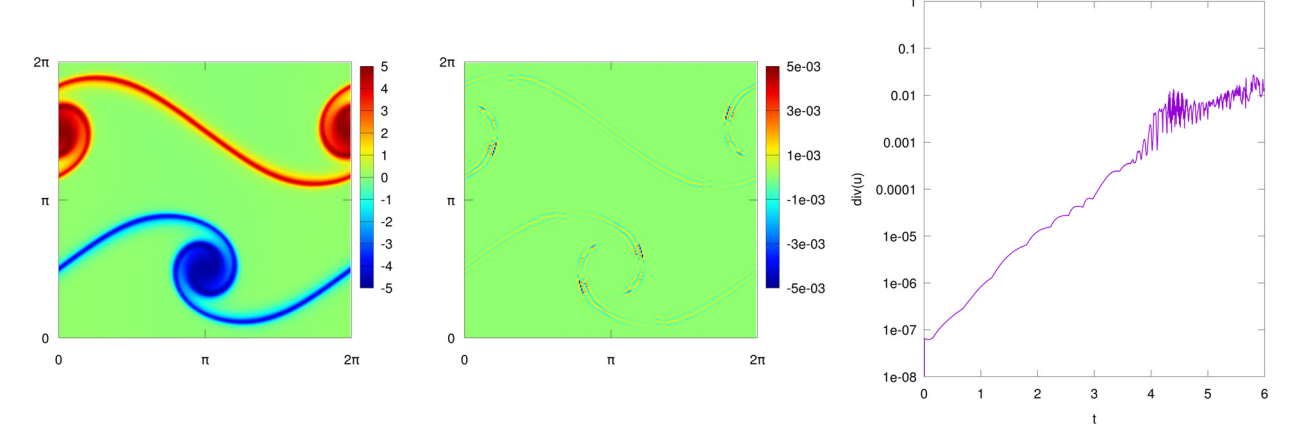


Fig. 5.11. Example 5.10. The vorticity $\omega = v_x - u_y$ (left), divergence $u_x + v_y$ (middle) for the shear flow problem at T = 6. Mesh grid: 256×256 . Right panel is the time history of L^{∞} norm of the divergence.

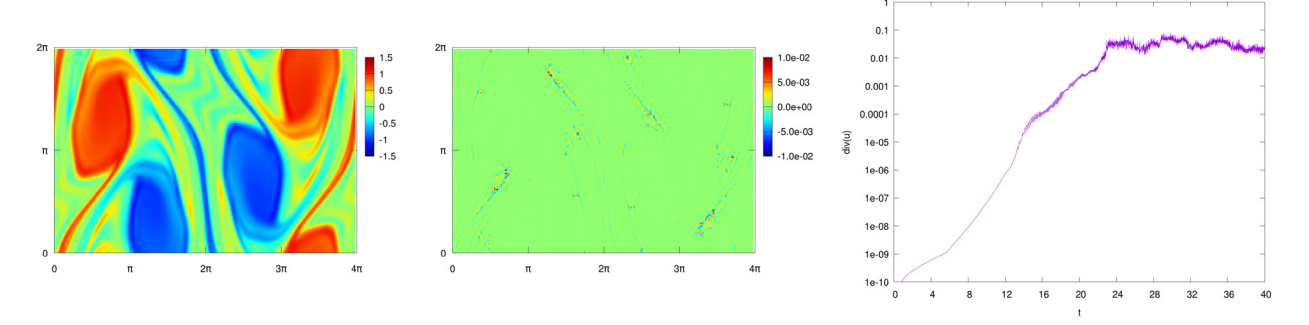


Fig. 5.12. Example 5.11. The vorticity $\omega = v_x - u_y$ (left) and divergence $u_x + v_y$ (middle) for the Kelvin-Helmholtz instability problem at T = 40. Mesh grid: 256×128 . Right panel is the time history of L^{∞} norm of the divergence.

6. Conclusion

In this paper we present high-order semi-implicit IMEX-WENO schemes for all-Mach isentropic Euler equations. The schemes are constructed by combining IMEX discretization in time with high order non-oscillatory space discretization in the finite difference framework. In particular, we use WENO discretization for the explicit (material) terms and central discretization for the implicit (acoustic) terms. The schemes are proven to be asymptotic accurate, i.e. they become consistent schemes for the limiting incompressible Euler equations with zero Mach number, and maintain the expected order of convergence. A detailed stability analysis shows that the schemes are linearly stable for Mach numbers less than one, under the material CFL restriction. The effectiveness of the approach is demonstrated by extensive numerical tests from the literature.

Our algorithm development serves as a first step in the direction of the construction of robust high order solvers for all Mach number flows. Future work consists of the following possibilities: (a) consideration of the full Euler system; (b) imposing exact incompressibility at the discrete level; (c) adaptive time stepping, (d) consideration of order reduction phenomenon for intermediate regimes of ε .

Appendix A. AP property for semi-implicit linearized SI IMEX-RK scheme

In this Appendix, we provide a proposition with proof for semi-implicit linearized SI IMEX-RK schemes, similar to the results presented in Section 4.

Proposition A.1. With the same assumptions as in Proposition 4.2, we consider applying a SI IMEX-RK scheme to system (2.2). Assume that the IMEX-RK method is SA, i.e. $b^T = e_s^T A$ with $e_s = (0, ..., 0, 1)^T$. Then we have, in the limit of $\varepsilon \to 0$, the incompressible condition (4.31). Furthermore, let $\mathbf{u}_{inc}(\mathbf{x}, t)$ be the exact solution of the incompressible Euler equations with initial data $\mathbf{u}_{inc}(\mathbf{x}, 0) = \mathbf{u}_0^0(\mathbf{x})$, then one has the one-step error estimate as specified in eq. (4.32).

Proof. We first recall that E as subscript denotes explicit variables, and I for the implicit ones. By (3.26) and (3.29), similar to corresponding equations (4.34) for NI IMEX-RK schemes, we have

$$\underline{\rho}_{I} = \rho^{0} \underline{e} - \Delta t A \nabla_{\mathbf{x}} \cdot \underline{\mathbf{q}}_{I},
\underline{\mathbf{q}}_{I} = \mathbf{q}^{0} \underline{e} - \Delta t A \left(\nabla_{\mathbf{x}} \cdot \underline{\mathbf{f}}_{E} + \frac{1}{\varepsilon^{2}} \underline{p}'_{E} \nabla_{\mathbf{x}} \underline{\rho}_{I} \right),$$
(A.1)

where $\underline{p}_E' = p'(\underline{\rho}_E)$ and $\underline{\mathbf{f}}_E := \underline{\mathbf{q}}_E \otimes \underline{\mathbf{q}}_E/\underline{\rho}_E$. We insert $\underline{\mathbf{q}}_I$ into the equation for $\underline{\rho}_I$ and get

$$\frac{\Delta t^2}{\varepsilon^2} A^2 \left(\nabla_{\mathbf{x}} \cdot \left(\underline{p}_E' \nabla_{\mathbf{x}} \underline{\rho}_I \right) \right) = (\underline{\rho}_I - \rho^0 \underline{e}) + \Delta t A \nabla_{\mathbf{x}} \cdot \mathbf{q}^0 \underline{e} - \Delta t^2 A^2 \nabla_{\mathbf{x}}^2 : \underline{\mathbf{f}}_E. \tag{A.2}$$

Plug the assumptions (4.36) into (A.2), we get, for the order $\mathcal{O}(\varepsilon^{-2})$,

$$\underline{p}'_{0,E}\nabla\underline{\rho}_{0,I}=0,$$

then by $p'_{0,E} \neq 0$, we have $\nabla \underline{\rho}_{0,I} = 0$, i.e., $\underline{\rho}_{0,I}$ is independent of space. Integrating the first equation in (A.1) over Ω and by considering the boundary conditions, we get $\underline{\rho}_{0,I} = \rho_0^0 \underline{e}$, i.e. $\underline{\rho}_{0,I}$ is independent of time.

By the hypothesis: $\nabla_{\mathbf{x}} \cdot \mathbf{q}_0^0 = \rho_0^0 \nabla_{\mathbf{x}} \cdot \mathbf{u}_0^0 = 0$, the $\mathcal{O}(1)$ term in ε for (A.2) yields:

$$\nabla_{\mathbf{x}} \cdot \left(\underline{p}_{\mathbf{0},E}' \nabla_{\mathbf{x}} \underline{\rho}_{\mathbf{2},I} \right) = -\nabla_{\mathbf{x}}^{2} : \underline{\mathbf{f}}_{\mathbf{0},E}. \tag{A.3}$$

Taking the divergence of $\underline{\mathbf{q}}_{0,I}$ for the $\mathcal{O}(1)$ term for the second equation in (A.1) and considering (A.3) we have $\nabla_{\mathbf{x}} \cdot \underline{\mathbf{q}}_{0,I} = 0$, then $\nabla_{\mathbf{x}} \cdot \underline{\mathbf{u}}_{0,I} = 0$.

By (4.33) we get for the numerical solution

$$\rho^{1} = \rho^{0} - \Delta t \underline{b}^{T} \nabla_{\mathbf{x}} \cdot \underline{\mathbf{q}}_{I},$$

$$\mathbf{q}^{1} = \mathbf{q}^{0} - \Delta t \underline{b}^{T} \left(\nabla_{\mathbf{x}} \cdot \underline{\mathbf{f}}_{E} + \frac{1}{\varepsilon^{2}} p_{E}' \nabla_{\mathbf{x}} \underline{\rho}_{I} \right).$$
(A.4)

For the $\mathcal{O}(1)$ term of the first subequation of (A.4), by $\nabla_{\mathbf{x}} \cdot \underline{\mathbf{q}}_{0,I} = 0$, it follows $\rho_0^1 = \rho_0^0$; for the $\mathcal{O}(1)$ term of the second subequation of (A.4) and by taking the divergence of \mathbf{q}_0^1 in (A.4), we get by (A.3),

$$\nabla_{\mathbf{x}} \cdot \mathbf{q}_{0}^{1} = \rho_{0}^{1} \nabla_{\mathbf{x}} \cdot \mathbf{u}_{0}^{1} - \Delta t \underline{b}^{T} \left(\nabla_{\mathbf{x}}^{2} : \underline{\mathbf{f}}_{0,E} + \nabla_{\mathbf{x}} \cdot \left(\underline{p}'_{0,E} \nabla_{\mathbf{x}} \underline{\rho}_{2,I} \right) \right) = \rho_{0}^{0} \nabla_{\mathbf{x}} \cdot \mathbf{u}_{0}^{1} = 0,$$

i.e., $\nabla \cdot \mathbf{u}^1(\mathbf{x}; \varepsilon) \to 0$ for $\varepsilon \to 0$. (4.31) and (4.32) can be proved in a similar fashion as in Proposition 4.2.

Note that if we consider *not well-prepared* initial data, for instance: $\nabla \cdot \mathbf{u}(\mathbf{x})_0^0 \neq \mathbf{0}$ with $\rho_0^0 = \text{Const.}$, from (A.2) we get for the $\mathcal{O}(1)$ term in ε

$$\Delta t \left(\nabla_{\mathbf{x}}^{2} : \underline{\mathbf{f}}_{0,E} + \nabla_{\mathbf{x}} \cdot \left(p_{0,E}' \nabla_{\mathbf{x}} \rho_{2,L} \right) \right) = A^{-1} \underline{e} \nabla_{\mathbf{x}} \cdot \mathbf{q}_{0}^{0}, \tag{A.5}$$

and from the second equation in (A.4), taking into account of the divergence for \mathbf{q}_0^1 , the $\mathcal{O}(1)$ term by (A.5) yields:

$$\nabla_{\mathbf{x}} \cdot \mathbf{q}_0^1 = (1 - b^T A^{-1} \underline{e}) \nabla_{\mathbf{x}} \cdot \mathbf{q}_0^0.$$

If the semi-implicit scheme has the property of SA, then it follows $1 - b^T A^{-1}\underline{e} = 0$, that is, we get again: $\nabla_{\mathbf{x}} \cdot \mathbf{q}_0^1 = 0$. Notice that for fully discrete scheme with spatial discretization, it is usually the case that $\nabla \cdot \mathbf{u}(\mathbf{x})_0^0 \neq \mathbf{0}$.

Appendix B. IMEX schemes

We provide several Butcher tableaux from literature for IMEX schemes of various types, with or without stiffly accurate (SA), globally stiffly accurate (GSA) properties, and of first, second and third order accurate.

• GSA DIRK(1,1,1) [1]

This method has order p = 1.

• SA SSP2(3,3,2) [34]

This method has order p = 2.

• GSA DIRK(2,2,2) [1]

where $\gamma = 1 - \frac{\sqrt{2}}{2}$ and $\delta = 1 - 1/(2\gamma)$. This method has order p = 2.

• SA DIRK(3,4,3) [1]

0	0	0	0	0	0	0	0	0	0	
γ	γ	0	0	0	γ	0	γ	0	0	
0.717933	0.3212788	0.396654	0	0	0.717933	0	0.282066	γ	0	(B.4)
1	0.321278	0.321278	0.396654	0	1	0	1.208496	-0.644363	γ	
	0	1.208496	-0.644363	γ		0	1.208496	-0.644363	γ	

with $\gamma = 0.435866$. This method has order p = 3.

SA DIRK(3,4,3)

with $\gamma = 0.435866$. This method has order p = 3.

• GSA DIRK(4,4,3) [1]

This method has order p = 3.

References

- [1] U.M. Ascher, S.J. Ruuth, R.J. Spiteri, Implicit-explicit Runge-Kutta methods for time-dependent partial differential equations, Appl. Numer. Math. 25 (1997) 151–167.
- [2] J.B. Bell, P. Colella, H.M. Glaz, A second-order projection method for the incompressible Navier-Stokes equations, J. Comput. Phys. 85 (1989) 257-283.
- [3] S. Boscarino, Error analysis of IMEX Runge-Kutta methods derived from differential-algebraic systems, SIAM J. Numer. Anal. 45 (2008) 1600-1621.
- [4] S. Boscarino, R. Bürger, P. Mulet, G. Russo, L.M. Villada, Linearly implicit IMEX Runge-Kutta methods for a class of degenerate convection-diffusion problems, SIAM J. Sci. Comput. 37 (2015) B305-B331.
- [5] S. Boscarino, R. Bürger, P. Mulet, G. Russo, L.M. Villada, On linearly implicit IMEX Runge-Kutta methods for degenerate convection-diffusion problems modeling polydisperse sedimentation, Bull. Braz. Math. Soc. (N.S.) 47 (2016) 171–185.
- [6] S. Boscarino, F. Filbet, G. Russo, High order semi-implicit schemes for time dependent partial differential equations, J. Sci. Comput. 68 (2016) 975–1001.
- [7] S. Boscarino, P.G. LeFloch, G. Russo, High-order asymptotic-preserving methods for fully nonlinear relaxation problems, SIAM J. Sci. Comput. 36 (2014) A377–A395.
- [8] S. Boscarino, J.-M. Qiu, G. Russo, On the implicit-explicit integral deferred correction methods for stiff problems, SIAM J. Sci. Comput. 40 (2) (2017) A787–A816, https://doi.org/10.1137/16M1105232.
- [9] S. Boscarino, G. Russo, On a class of uniformly accurate IMEX Runge-Kutta schemes and applications to hyperbolic systems with relaxation, SIAM J. Sci. Comput. 31 (2009) 1926–1945.
- [10] S. Boscarino, G. Russo, Flux-explicit IMEX Runge-Kutta schemes for hyperbolic to parabolic relaxation problems, SIAM J. Numer. Anal. 51 (2013) 163–190.
- [11] S. Boscarino, G. Russo, L. Scandurra, All Mach number second order semi-implicit scheme for the Euler equations of gas dynamics, J. Sci. Comput. (2017) 1–35.
- [12] V. Casulli, D. Greenspan, Pressure method for the numerical solution of transient, compressible fluid flows, Int. J. Numer. Methods Fluids 4 (1984) 1001–1012.
- [13] A.J. Chorin, Numerical solution of the Navier-Stokes equations, Math. Comput. 22 (1968) 745-762.
- [14] B. Cockburn, C. Johnson, C.-W. Shu, E. Tadmor, in: Advanced Numerical Approximation of Nonlinear Hyperbolic Equations: Lectures Given at the 2nd Session of the Centro Internazionale Matematico Estivo (CIME) Held in Cetraro, Italy, June 23–28, 1997, Springer, 2006.
- [15] P. Colella, K. Pao, A projection method for low speed flows, J. Comput. Phys. 149 (1999) 245-269.
- [16] F. Cordier, P. Degond, A. Kumbaro, An asymptotic-preserving all-speed scheme for the Euler and Navier-Stokes equations, J. Comput. Phys. 231 (2012) 5685–5704.

- [17] N. Crouseilles, M. Mehrenberger, E. Sonnendrücker, Conservative semi-Lagrangian schemes for Vlasov equations, J. Comput. Phys. 229 (2010) 1927–1953.
- [18] J. de Frutos, V. John, J. Novo, Projection methods for incompressible flow problems with WENO finite difference schemes, J. Comput. Phys. 309 (2016) 368–386
- [19] P. Degond, M. Tang, All speed scheme for the low Mach number limit of the isentropic Euler equations, Commun. Comput. Phys. 10 (2011) 1–31.
- [20] S. Dellacherie, Analysis of Godunov type schemes applied to the compressible Euler system at low Mach number, J. Comput. Phys. 229 (2010) 978–1016.
- [21] G. Dimarco, R. Loubère, M.-H. Vignal, Study of a new asymptotic preserving scheme for the Euler system in the low Mach number limit, SIAM J. Sci.
- [22] E. Godlewski, P.-A. Raviart, Numerical Approximation of Hyperbolic Systems of Conservation Laws, Springer, 2014.
- [23] P. Gresho, On the theory of semi-implicit projection methods for viscous incompressible flow and its implementation via finite-element method that also introduces a nearly consistent mass matrix. Part 2: Implementation, Int. J. Numer. Methods Fluids 11 (1990) 621–659.
- [24] J.-L. Guermond, P. Minev, J. Shen, An overview of projection methods for incompressible flows, Comput. Methods Appl. Mech. Eng. 195 (2006) 6011–6045.
- [25] J. Haack, S. Jin, J.-G. Liu, An all-speed asymptotic-preserving method for the isentropic Euler and Navier-Stokes equations, Commun. Comput. Phys. 12 (2012) 955–980.
- [26] E. Hairer, G. Wanner, Solving Ordinary Differential Equations II: Stiff and Differential Algebraic Problems, vol. 2, Springer Verlag, 1993.
- [27] J. Kim, P. Moin, Application of a fractional-step method to incompressible Navier-Stokes equations, J. Comput. Phys. 59 (1985) 308-323.
- [28] S. Klainerman, A. Majda, Singular limits of quasilinear hyperbolic systems with large parameters and the incompressible limit of compressible fluids, Commun. Pure Appl. Math. 34 (1981) 481–524.
- [29] R. Klein, Semi-implicit extension of a Godunov-type scheme based on low Mach number asymptotics. I: One-dimensional flow, J. Comput. Phys. 121 (1995) 213–237.
- [30] H.P. Langtangen, K.-A. Mardal, R. Winther, Numerical methods for incompressible viscous flow, Adv. Water Resour. 25 (2002) 1125-1146.
- [31] R.J. LeVeque, Finite Volume Methods for Hyperbolic Problems, vol. 31, Cambridge University Press, 2002.
- [32] F. Miczek, F. Röpke, P. Edelmann, A new numerical solver for flows at various Mach numbers, Astron. Astrophys. 576 (2015) A50.
- [33] C.-D. Munz, S. Roller, R. Klein, K.J. Geratz, The extension of incompressible flow solvers to the weakly compressible regime, Comput. Fluids 32 (2003) 173–196.
- [34] L. Pareschi, G. Russo, Implicit-explicit Runge-Kutta schemes and applications to hyperbolic systems with relaxation, J. Sci. Comput. 25 (2005) 129-155.
- [35] F. Rieper, A low-Mach number fix for Roe's approximate Riemann solver, J. Comput. Phys. 230 (2011) 5263-5287.
- [36] C.-W. Shu, High order weighted essentially nonoscillatory schemes for convection dominated problems, SIAM Rev. 51 (2009) 82-126.
- [37] M. Tavelli, M. Dumbser, A pressure-based semi-implicit space-time discontinuous Galerkin method on staggered unstructured meshes for the solution of the compressible Navier-Stokes equations at all Mach numbers, J. Comput. Phys. 341 (2017) 341–376.
- [38] E.F. Toro, Riemann Solvers and Numerical Methods for Fluid Dynamics: A Practical Introduction, Springer, 2009.
- [39] E. Turkel, Preconditioned methods for solving the incompressible and low speed compressible equations, J. Comput. Phys. 72 (1987) 277-298.
- [40] C. Viozat, Implicit Upwind Schemes for Low Mach Number Compressible Flows, PhD thesis, Inria, 1997.
- [41] X. Zhong, Additive semi-implicit Runge-Kutta methods for computing high-speed nonequilibrium reactive flows, J. Comput. Phys. 128 (1996) 19-31.
- [42] H. Zhu, J. Qiu, J.-M. Qiu, An h-adaptive RKDG method for the two-dimensional incompressible Euler equations and the guiding center Vlasov model, J. Sci. Comput. (2017) 1–22.